energies

MDPI

Review

Methane Cracking for Hydrogen Production: A Review of Catalytic and Molten Media Pyrolysis

Malek Msheik, Sylvain Rodat and Stéphane Abanades *

Processes, Materials and Solar Energy Laboratory, PROMES-CNRS, 7 Rue du Four Solaire, 66120 Font Romeu, France; malek.msheik@promes.cnrs.fr (M.M.); sylvain.rodat@promes.cnrs.fr (S.R.)
* Correspondence: stephane.abanades@promes.cnrs.fr; Tel.: +33-(0)4-68-30-77-30

Abstract: Currently, hydrogen is mainly generated by steam methane reforming, with significant CO_2 emissions, thus exacerbating the greenhouse effect. This environmental concern promotes methane cracking, which represents one of the most promising alternatives for hydrogen production with theoretical zero CO/CO_2 emissions. Methane cracking has been intensively investigated using metallic and carbonaceous catalysts. Recently, research has focused on methane pyrolysis in molten metals/salts to prevent both reactor coking and rapid catalyst deactivation frequently encountered in conventional pyrolysis. Another expected advantage is the heat transfer improvement due to the high heat capacity of molten media. Apart from the reaction itself that produces hydrogen and solid carbon, the energy source used in this endothermic process can also contribute to reducing environmental impacts. While most researchers used nonrenewable sources based on fossil fuel combustion or electrical heating, concentrated solar energy has not been thoroughly investigated, to date, for pyrolysis in molten media. However, it could be a promising innovative pathway to further improve hydrogen production sustainability from methane cracking. After recalling the basics of conventional catalytic methane cracking and the developed solar cracking reactors, this review delves into the most significant results of the state-of-the-art methane pyrolysis in melts (molten metals and salts) to show the advantages and the perspectives of this new path, as well as the carbon products' characteristics and the main factors governing methane conversion.

Keywords: methane cracking; H_2 production; conventional catalysts; deactivation; regeneration; molten metals/salts pyrolysis; heat transfer; concentrated solar energy; carbon characteristics

Citation: Msheik, M.; Rodat, S.; Abanades, S. Methane Cracking for Hydrogen Production: A Review of Catalytic and Molten Media Pyrolysis. *Energies* **2021**, *14*, 3107. https://doi.org/10.3390/en14113107

Academic Editor: Abdul-Ghani Olabi

Received: 16 April 2021
Accepted: 22 May 2021
Published: 26 May 2021

1. Introduction

The continuous and ubiquitous use of fossil fuels as an energy source has raised serious concerns around the depletion of these resources and their associated greenhouse gas emissions. Moreover, the need for additional energy has driven researchers to develop new sustainable processes that yield cleaner and more environmentally friendly fossil fuel alternatives, especially hydrogen. Hydrogen production for fuel has taken several pathways that include steam methane reforming (SMR), partial oxidation of hydrocarbons, methane cracking, coal gasification, and water electrolysis [1,2]. However, most of these processes are CO/CO_2 emitting, except methane cracking or electrolysis when powered by solar energy [3].

Although SMR produces more hydrogen per mole of methane than other routes (Equation (1)), CO_2 emissions are still the main drawback [4]. CO_2 has to be captured and confined underground in depositories in outlying unpopulated areas (known as carbon capture and sequestration (CCS)), which implies additional costs to the process [5]. Moreover, current CO_2 sequestration techniques are not efficient enough for long-term and safe storage [5].

$$CH_{4_{(g)}} + 2H_2O_{(l)} \rightarrow CO_{2_{(g)}} + 4H_{2_{(g)}} \qquad \Delta H^0_{25\,^\circ C} = 252.75\ \text{kJ/mol of}\ CH_4 \qquad (1)$$

In the long term, all hydrogen production could come from water splitting (electrolysis, photo-electrolysis, or thermolysis via multistep cycles) (Equation (2)), as it is a zero CO/CO_2-emitting process if based on a renewable resource (e.g., wind, solar, etc.) [6]. However, nowadays, water electrolysis is still uneconomical enough to supplant other H_2 production pathways. It only contributes to 4% of the total worldwide hydrogen production because of the high production cost (3.19 EUR/kg H_2 for the cheapest water electrolysis using wind energy against 1.87 EUR/kg H_2 and 1.71 EUR/kg H_2 for SMR with and without CO_2 sequestration, respectively) [7].

$$2H_2O_{(l)} \rightarrow 2H_{2_{(g)}} + O_{2(g)} \qquad \Delta H^0_{25\,^\circ C} = 285.8\ \text{kJ/mol of } H_2O \tag{2}$$

Although nowadays most hydrogen is being produced via CO/CO_2-emitting technologies (48% from SMR, 30% from partial oxidation of hydrocarbons, 18% from coal gasification) [3,8], methane cracking has recently grabbed special attention because it is a zero CO/CO_2-emitting process (Equation (3)). Hence, methane cracking cancels the need for CCS. The only byproduct recovered with the hydrogen is the solid carbon that is normally valuable and could be commercialized after purification. Thereafter, it can be used in many applications, such as double-layer capacitors, polymers (e.g., rubber reinforcement for the tire industry), carbon nanofiber-based composites, precursors of graphitic materials to be used as anodes in Li-ion batteries, etc. [9]. However, the current carbon market is still highly limited and most carbon byproduct has to be stored until new applications are found [10].

$$CH_{4_{(g)}} \rightarrow C_{(s)} + 2H_{2(g)} \qquad \Delta H^0_{25\,^\circ C} = 74.85\ \text{kJ/mol of } CH_4 \tag{3}$$

Methane cracking is an endothermic reaction that takes place at high temperatures. Once the temperature is higher than 300 °C, methane theoretically starts to decompose into solid carbon particles and H_2 gas without any catalyst, according to thermodynamics. Nevertheless, for a noncatalytic methane cracking, a reasonable high conversion can hardly be reached below 1200 °C due to kinetic limitations and to the high activation energy required to break stable C–H bonds of methane molecules [11]. This activation energy varies in the literature. For example, Rodat et al. [12] reported 370 kJ/mol against 422 kJ/mol, according to Keipi et al. [13]. Other authors found that it is comprised between 356 and 452 kJ/mol [14–17]. Thus, catalyst addition can significantly decrease this activation energy to the range of 205–236 kJ/mol for carbonaceous catalysts and even lower for solid transition metals such as unsupported Ni (96.1 kJ/mol). Consequently, catalytic methane decomposition occurs at a temperature in the range of 600–900 °C, which is similar to that of SMR [18].

Therefore, regarding methane cracking, one of the key parameters is the catalyst type that may undergo deactivation by coke deposition on its active sites. Many experimental studies have been achieved in the last decades using metallic, especially transition, metals (Ni, Fe, Co, Cu, etc.) [19–22], and carbonaceous catalysts [23–27] to reduce the activation energy of the reaction. Although some of these catalysts have good catalytic activities, they often deactivate by coking. Some metals, such as Ni, are expensive, and, as regeneration is not ideal, it is almost impossible to recover the initial activity of the catalyst due to surfaces and pores deformation and traces of carbon impurities that persist inside [28]. Although carbonaceous catalysts do not theoretically necessitate regeneration, their catalytic activity also drops after a few hours of operation [18]. Furthermore, whether the methane pyrolysis is catalyzed or not, a frequently encountered problem is the accumulative coke deposition on the hot walls of the reactor, which may completely clog it after a few hours of operation. This problem hinders the continuity and the scalability of the process.

To address catalyst deactivation issues in conventional methane cracking, pyrolysis in molten media was suggested in the early twentieth century by Daniel Tyrer [29]. It came to light again in 1999 when Steinberg [30] proposed hydrocarbon pyrolysis in molten tin as a heat transfer medium. The concept is based on methane bubbling in a molten medium.

While they are rising, methane bubbles decompose under the high-temperature effect of the melt (Sn, Bi, Al, etc.). H_2 leaves as the effluent gas while carbon particles float at the melt surface, driven by buoyancy forces. Consequently, reactor blockage due to carbon deposition on the reactor walls can be efficiently prevented [31].

Initially, the liquid phase was not meant to catalyze the reaction. It was supposed to prohibit carbon sticking to the hot reactor walls and to enhance the heat transfer due to the high heat capacities of molten metals/salts. However, investigations concerning the catalytic performance of molten media have also taken place. While most active metal catalysts (Ni, Pd, Pt, etc.) have high melting points (>1000 °C), most inert metals (Sn, Bi, Ga, In, etc.) have low melting points (200–700 °C). Because the latter ones exhibit negligible catalytic activity, such as pure Sn melt [3,8,32], alloys composed of active and inert metals are used for pyrolysis while expecting a good conversion [33].

First of all, this review recalls the basics of conventional methane cracking, using solid metallic and carbonaceous catalysts, with the relevant catalyst issues. Then, it highlights the main studies on solar methane cracking, which could be a promising pathway for CO_2-free hydrogen production. Thereafter, the most significant and recent results of methane cracking in molten media are elaborated upon to show the advantages and the perspectives of this new route. In the end, reaction kinetics modeling, carbon product characteristics, and the main influencing factors affecting methane pyrolysis are discussed.

2. Conventional Catalytic Methane Pyrolysis

Independently from the means of heating in methane pyrolysis (e.g., concentrated solar energy or electrical heating), catalysts are useful for boosting methane decomposition at temperatures below 1000 °C, thus lowering the complexity and the cost of the process. Therefore, different catalysts have been used to investigate methane pyrolysis [18,19,34–40], including solid metal and carbonaceous catalysts, and molten media (metals or salts). As a new path, cracking in molten media is the particular originality of this review and is discussed in a dedicated part. The following section reviews the basic concepts and the challenges of conventional catalyzed methane cracking.

2.1. Solid Metallic Catalysts

Metals used in catalytic methane cracking are numerous. Some of them have proved to be active catalysts, while others have shown poor performance, and then were considered as inert metals. Active metals used in methane cracking are (Ni, Pd, Pt) [41–45] and (Fe, Co) [46,47], which are often supported on metal oxides such as Al_2O_3, MgO, SiO_2, and TiO_2. Ni, Co, and Fe have been extensively experimented with, in particular, due to their relative abundance and lower prices compared with noble metals. The performance of Ni is the highest, followed by Co, and then Fe [47–51]. Generally speaking, these transition metals offer the best activity because their 3d orbitals are partially filled, making it possible to receive electrons from C–H bonds, thereby facilitating the decomposition mechanism [22,34,52].

Although Ni has shown the best catalytic activity among conventional transition metals [44,46], it quickly deactivates above 600 °C because the solid carbon byproduct encapsulates its active sites [26,41,53–56]. Co has also a good performance, but it is even more expensive and more toxic than Ni [57]. Therefore, Co-contaminated carbon is not safe if not purified. This toxicity issue is unfavorable because the current carbon market is still limited, and in the objective of carbon sequestration, most of the produced material should be permanently stored. Fe, a cheaper and nontoxic metal with an acceptable activity, could be a potential candidate for industrial-scale application [58]. Fe is also more resistant to deactivation [59], and more stable at high temperatures than Ni and Co. This is probably due to the low carbon solubility and higher carbon diffusion through the pores of Fe [59,60]. Explicitly, at high temperatures, when the conversion is higher, the carbon production increases in parallel, necessitating a high diffusion rate through the catalyst pores to resist coking. Fe, which originally offers higher carbon diffusion capacity through its pores,

is then considered more resistant to deactivation at high temperatures than Ni and Co. Additionally, these transition metals are known to form carbon nanotubes or fibers through the carbon atom supersaturation–precipitation mechanism, which is also dependent on temperature and metal particle size. Generally, for most catalysts, deactivation occurs after the bulk/surface is saturated, whether or not the catalyst has a high diffusivity for carbon.

However, to enhance the catalyst performance, metals are usually prepared as a matrix consisting of the active metal dispersed on supports such as carbon nanofibers (CF), SiO_2, TiO_2, Al_2O_3, MgO, etc. [41,47,61,62]. The support can help to hinder the catalyst agglomeration, and hence offers a higher surface area for methane dissociation.

2.1.1. Role of Metal Catalyst Supports

The support has a significant impact on the catalytic activity and the catalyst lifetime [63,64]. The interaction between the metal particles and the support is a critical factor. A good interaction allows a better dispersion of the metal particles on the support, which prevents the agglomeration and the sintering of the metal particles [34]. As a result, the activity is enhanced due to better dispersion and reducibility of the metal species. However, a very strong interaction may have a negative influence on the performance of the catalyst. An excessive interaction can indeed result in the formation of hardly-reducible metal–support species, and hence hinders the formation of the metallic active sites [46].

Ermakova et al. [46] investigated the difference between magnesia and silica supports for Ni catalyst. They found that silica performed better, mainly because nickel silicate is unstable, unlike the solid solution of nickel with magnesium formed in the presence of magnesia support. Fe/SiO_2 and Ni/SiO_2 were also investigated [65]. The silicate presence showed negative effects on the performance of Ni but enhanced that of Fe, depending on the amount of silicate within the catalyst. This means that the support was suitable for Fe but not for Ni. Takenaka et al. [41] studied the activity of Pd–Ni alloy on different supports. They found that carbon-based supports were always the best, even for either pure Ni or pure Pd metal catalyst. Briefly, they found the following activity order: carbon nanofibers > TiO_2 > SiO_2 > Al_2O_3. Thus, a moderate metal–support interaction should be found to enhance the catalytic activity and to prevent any early deactivation [34].

To further enhance the stability and the performance of metal catalysts and to delay their deactivation, other metals can be added to the principal active catalyst that is often supported. These metals are called promoters.

2.1.2. Role of Metal Catalyst Promoters

To enhance the catalytic performance and the lifetime of metallic catalysts, some researchers incorporated another metal herein [41–43,45,66]. A promoter metal is then blended with the main metallic catalyst. This metal matrix usually forms a metal alloy, offering a higher surface area for methane dissociation. The alloy provides more active sites for methane dissociation, allowing enhanced access and diffusion of the carbon byproduct particles through the pores, and hence reducing the carbon deposition on the active sites. Subsequently, the encapsulation of the active sites by the carbon byproduct is prevented or delayed. Thus, the catalyst lifetime is prolonged. Moreover, the metal promoter improves the dispersion of the metallic catalyst on the support and enhances the metal reducibility. This may be directly related to the so-called hydrogen spillover effect implied by the metal promoter [34].

Takenaka et al. [41] showed that among several catalysts (Cu, Rh, Pd, Ir, and Pt), only Pd enhanced the catalytic activity and the lifetime of Ni on a carbon nanofiber support. They also claimed that Pd mixed with Ni (Pd/Ni molar ratio = 0.5) forms a metal alloy of Ni–Pd that increases the available active sites for methane molecules, resulting in higher hydrogen yield. However, copper was reported as an effective promoter for the catalytic activity of Ni La_2O_3-doped catalyst [67]. The catalyst alloy included small amounts of Al inside. With copper, Ni–Al reaction (known to form nickel aluminate) was inhibited, allowing for a higher available nickel surface for methane dissociation.

Despite their efficiency in deactivation resistance, metal supports and metal promoters do not ultimately inhibit the metal catalyst deactivation. Still, they only help to delay it as much as possible. In other words, they only extend the catalyst lifetime before complete deactivation.

2.1.3. Metal Catalysts Deactivation

There is no doubt that, ultimately, metal catalysts investigated in methane cracking undergo complete deactivation. Several deactivation mechanisms can modify the performance of the catalyst, such as fouling, coking, poisoning, mechanical degradation, etc. [68,69]. In methane cracking, the catalyst activity is mainly influenced by coking [69]. The coke is the excessive carbon being produced during the reaction that blocks access to the active sites of the catalyst.

Catalysts differ by their capacities to allow carbon diffusion through their pores, which could be defined as a catalyst characteristic. The diffusion behavior of carbon atom in a metal is determined by both solubility and diffusivity. They are both dependent on temperature and other operating conditions, such as pressure [70].

Some authors state that for a given catalyst, before deactivation, there is usually an equilibrium settling between the carbon production rate and the carbon solubility and diffusion through catalyst pores. Once the reaction rate increases (e.g., if the temperature is raised), the carbon production may become excessive, and the amount of coke surrounding the catalyst can overload its capacity to allow diffusion. Thus, the aforementioned equilibrium is broken, and carbon starts to depose on and around the active sites of the catalyst. This coking inhibits the adsorption of methane molecules on the active sites, leading to a gradual deactivation and a conversion drop. Moreover, the catalyst encapsulation decreases the heat transfer rate toward the metal particle bulk, then lowers the diffusion rate through the pores and fastens the deactivation [71].

Coke deposition may occur in different manners. Carbon can fill the pores or cover the surface of the catalyst, hence blocking access of the reacting gas to the active sites. It can also deposit around the active sites, blocking access to them again. A third way is the formation of hard carbon tubes leading to the catalyst disintegration [69,72].

Catalysts with originally higher carbon diffusion capacities and lower carbon solubilities are more resistant to deactivation when the pyrolysis is conducted at high temperatures. This may be the case for Fe that operates well at temperatures between 700 and 900 °C, unlike Ni and Co that undergo deactivation at lower temperatures [59,60].

However, even for catalysts with longer lifetimes (e.g., Fe), the resistance against deactivation is still limited. When the reaction rate is very high, the carbon overwhelms the catalyst bulk, and gradual deactivation occurs. Once the catalyst is fully deactivated, the performance drops drastically, accompanied by a sharp decrease in conversion. Consequently, the process must be shut down to change the catalyst or to conduct a regeneration step to recover the catalytic activity. Generally, a deactivated metal catalyst is regenerable by different methods, but with some associated drawbacks.

2.1.4. Metal Catalysts Regeneration

Metallic catalysts require regeneration to recover most of their initial activity. There are mainly three methods to regenerate metallic catalysts: (i) steam regeneration that yields hydrogen and carbon monoxide (Equation (4)), (ii) air regeneration that yields carbon monoxide or carbon dioxide depending on the excess air being fed (Equations (5) and (6)), and (iii) carbon dioxide regeneration that yields carbon monoxide (Equation (7)) [18,73]. The most common methods are steam and air regeneration.

Energetically speaking, when O_2 is concomitantly fed with methane, air regeneration is a suitable method to compensate some of the energetic requirements of methane cracking, as it is an exothermic reaction, unlike endothermic steam regeneration [74]. Moreover, it is faster than steam regeneration. However, it has been reported that the high temperature during carbon oxidation may disintegrate the catalyst into powder [61,75].

Villacampa et al. [76] reported the activity loss of Ni/Al_2O_3 catalyst after the first air regeneration, mainly due to the sintering of the active sites. Rahman et al. [75] assigned the loss of activity of Ni/Al_2O_3 to the disintegration and the morphology modification of the catalyst. However, partial oxidation of the catalyst may efficiently lead to the recovery of some of the catalytic activity. Koç et al. [77] demonstrated that the partial oxidation of 5 wt.% Ni/Al_2O_3 could help recover a significant activity. In contrast, the complete oxidation resulted in drastic catalytic performance losses.

On the other hand, steam regeneration seems more efficient (in terms of catalytic activity recovery) and produces additional hydrogen as a valuable byproduct. Aiello et al. [78] showed that 15 wt.% Ni/SiO_2 was completely regenerated at 650 °C by steam for ten successive cracking/deactivation runs without any significant decrease in the activity. Zhang et al. [61] stated that both air and steam regeneration allowed recovery of most of the catalyst activity. However, although air oxidation was faster, it collapsed the bed into powder due to the high temperature during oxidation. Steam regeneration did not change the morphology of the bed, and contributed to more hydrogen production, which could be of significant interest.

$$C_{(s)} + H_2O_{(g)} \rightarrow CO_{(g)} + H_{2(g)} \qquad \Delta H^0_{25\,^\circ C} = +131.39\ kJ/mol \tag{4}$$

$$C_{(s)} + O_{2(g)} \rightarrow CO_{2(g)} \qquad \Delta H^0_{25\,^\circ C} = -393.78\ kJ/mol \tag{5}$$

$$2C_{(s)} + O_{2(g)} \rightarrow 2CO_{(g)} \qquad \Delta H^0_{25\,^\circ C} = -221.2\ kJ/mol \tag{6}$$

$$C_{(s)} + CO_{2(g)} \rightarrow 2CO_{(g)} \qquad \Delta H^0_{25\,^\circ C} = +172.58\ kJ/mol \tag{7}$$

Despite their low cost and high efficiency in some cases, these methods are CO/CO_2 emitting. Therefore, other regeneration techniques should be developed to keep the green asset of methane cracking. Meanwhile, and until more reliable regeneration techniques are developed, carbonaceous catalysts have received specific attention as they are low in cost, more resistant against deactivation, and do not theoretically necessitate regeneration.

2.2. Carbonaceous Catalysts

Different types of carbonaceous catalysts, such as activated char [24], biochar [24], coal char [27], carbon black [23,79], etc., have been studied for methane pyrolysis. They present several advantages over metallic catalysts: (i) lower cost, (ii) higher resistance to high temperature, (iii) safe storage, (iv) tolerance to impurities as sulfur, (v) no contamination of the carbon byproduct, (vi) generally no need for regeneration, (vii) additional self-catalytic effects of the produced carbon, and (viii) mitigation of CO_2 emissions, compared with metals, because the regeneration of metallic catalysts requires burning of the C on their surfaces which emits CO/CO_2 [24,80,81].

However, the catalytic performance itself is lower than that of metallic catalysts [53,82]. Although their activity drops after a few hours, due to modifications in the morphology and to pores blockage, unlike metals, it stabilizes after the initial drop in conversion. This is mainly because the produced carbon has also some catalytic activity (autocatalysis), which compensates the partial hindering of the active sites of the carbonaceous catalysts [23,24].

Several factors explain the difference between the catalytic activities: it has been found that if the same types of catalysts are used (e.g., if they are all activated carbons), then the higher the total specific surface area, the higher the conversion of methane that is obtained. In other words, catalysts with smaller pore diameters, represented by a smaller micropore volume, have a higher number of pores and hence a larger surface area. This leads to higher methane conversions [24,34]. However, if they are not of the same type (e.g., activated carbon against graphite), the dislocations and defects are the main factors affecting the catalytic performance, and it is commonly accepted that the defects are the active sites responsible for raising the catalyst activity [34,53]. In this case, the performance of catalysts of different types cannot be directly correlated to their specific surface area.

The surface composition may also influence the methane dissociation. It has been reported that oxygen-containing carbonaceous catalysts (R–COOH, R–OCO, R–OH, R=O, etc.) lead to higher conversions because oxygen functions activate C–H bonds to form CO_x [24,79,80]. Carbons containing oxygenated groups may thus lead to the presence of small amounts of CO in the effluent gas. Pyrolysis over activated carbon, known as oxygen-containing groups, led to 0.77 vol.% CO in the outlet gas, while the H_2-pretreated activated carbon only yielded 0.17 vol.% CO. However, the removal of oxygen groups slightly affects the hydrogen yield [80].

2.2.1. Role of Carbon Structure and Composition

Carbonaceous catalysts are mainly classified into three categories based on their crystallinity: highly ordered (graphite, diamond), less-ordered (glassy carbon, fullerene soot, fullerene $C_{60/70}$, carbon nanotubes, and ordered mesoporous carbons), and disordered carbons (amorphous, microcrystalline, such as coal char, carbon black, activated carbon, and acetylene carbon) [38]. Disordered carbons present a dislocated arrangement of C–H bonds, leading to dislocations, vacancies, low-coordination sites, atoms with free valences, discontinuities, edges, defects, and other abnormalities. These are usually called high-energy sites (HES). The more HES there are, the higher the initial activity. Therefore, the activity of carbonaceous catalysts is as follows: disordered carbons > less ordered (turbostratic) > highly ordered carbons [80]. In literature, most studies concern disordered carbons, especially activated carbon and carbon black, since they offer the best catalytic performance.

Muradov et al. [80] reported a higher initial activity of activated carbon compared with that of carbon black (for a comparable specific surface area). They stated that two types of impurities are present in carbon catalysts: metals (Fe, Ni, Co, etc.) and oxygen groups (carboxylic, lactonic, carbonyl, etc.) [83]. The trace amounts of metals determined by atomic absorption spectroscopy (AAS) provided no evidence of any role of metal impurities in the performance of the carbonaceous catalyst. However, oxygen group percentage determined by X-ray photoelectron spectroscopy (XPS) was reported to have a slightly positive influence on the performance of carbon black. Oxygen presence in carbons may come from either the manufacturing procedure or from carbon oxidization by air or steam. Activated carbon has been demonstrated to exhibit much more oxygen content than carbon black (almost 9 to 15 times) [80]. The oxygen content in the former increases in parallel with increasing specific surface area. In view of the higher catalytic performance of activated carbons compared with carbon blacks, the oxygen role may justify this behavior to some extent. Although this hypothesis was reported by many other authors [24,79], the whole difference in performance between the activated carbon and the carbon black cannot be only assigned to the presence of the oxygen groups. For example, regarding the family of activated carbons coming from petroleum coke and prepared by KOH activation, the positive oxygen influence on the catalyst performance was not observed. Activated carbons with higher oxygen content and higher surface area did not yield higher methane decomposition [80].

Serrano et al. [84] compared the activities of activated carbon and carbon black. Activated carbon offered a higher initial activity but deactivated quickly, while carbon black showed stable performance. They attributed this result to the higher surface area and the higher number of defects of activated carbon, which boosted the conversion in the beginning. However, with an extended time, the micropores were completely blocked, which could be seen as a drop in performance. Carbon black, having a smaller surface area and a higher graphene order, showed lower initial activity; however, the material was more resistant to deactivation for a longer operation. Savankumar et al. [24] investigated the catalytic activities of activated char and biochar. They found that activated char had higher initial activity due to the higher specific surface area (and higher number of pores). They reported stability in conversion after two drops, mainly because the carbon product acts as an additional catalyst (autocatalysis). However, at an extended operating time, biochar overperformed the activity of activated char since the latter exhibits a faster deactivation.

Although carbonaceous catalysts are more stable in term of performance and resistance to deactivation at high-temperature operations, they eventually undergo deactivation, just as metals do. The same coking mechanism that reduces the performance of metals also affects carbonaceous catalysts.

2.2.2. Carbon Deactivation

The main mechanism of carbon catalysts deactivation is the deposition of the carbon product on the surface, and hence the blockage of the pores mouth and the access to the active sites [85,86]. Therefore, the available active surface for methane dissociation is reduced, leading to a drop in the conversion.

During methane dissociation, there are two steps of carbon product formation: the first step is the formation of carbon nuclei that displays a good catalytic activity, followed by carbon-crystallites that are more ordered, thus having a lower activity and a higher volume. Both carbon types fill the pores of carbonaceous catalysts and diminish the conversion gradually. Considering that a pore has not a perfect structure, it usually includes both narrow and large paths. Therefore, the narrow parts are more likely to be blocked by the larger carbon particles, more particularly by the carbon crystallites [87].

Lázaro et al. [88] reported a decrease in the surface area of carbon black catalysts to 23% of the initial area in the first 120 min, then a slower decline to almost zero after 900 min. In contrast, the surface area of activated carbon diminished more sharply. They justified this result by the more open surface of carbon black (pores of larger diameters), which is easier accessed by methane molecules. In fact, carbon black has bigger but fewer pores than activated carbon, leading to a smaller surface area. However, the smaller surface area makes it more open than that of activated carbon. In contrast, activated carbon with smaller pores (higher surface area) has a relatively closed surface. Therefore, the crystallite carbon adheres to the catalyst's external surface and readily blocks all the pores. Generally, the drop in the catalytic activity of carbons was proportional to the decrease in their surface area [88–90].

Krzyzyński et al. [91] studied the deactivation of several activated carbons from the same precursor, prepared differently by activation with different weight ratios of KOH to precursor. They found that those with a higher surface area were the most resistant to deactivation. They also stated that carbonaceous catalysts with a higher surface area were the most suitable to overcome deactivation. However, this analysis should not be applied when comparing different types of carbon catalysts (activated carbon, carbon black, etc.), because of the opposite conclusion drawn by Lázaro et al. [88].

Although they do not necessitate regeneration due to their relatively low cost, carbon materials can still be partially regenerated to recover some of the initial catalytic activity.

2.2.3. Carbon Regeneration

The relatively lower cost of carbon catalysts compared with metals was one of the main advantages that motivated their use in methane cracking. Unlike metals, deactivated carbons do not imply high economic losses or toxicity issues. Therefore, regeneration is not as essential as for metal catalysts. Nonetheless, many researchers applied regeneration for carbons. Carbon regeneration techniques are precisely the same as those used for metals since the coking deactivation mechanism is quite similar.

Abbas and Daud [92] used CO_2 to recover some of the catalytic activity of activated carbon. Five CO_2 regenerations were achieved for six subsequent methane pyrolysis runs at 850 °C and 950 °C. They reported a decrease in the initial activity and the mass gain of the catalyst after each (pyrolysis + regeneration) cycle. However, the activity loss was lower at higher regeneration temperatures. Sun et al. [93] used oxygen to regenerate the char after the drop in hydrogen yield from 63 to 12% in 180 min. A content of 0.46% O_2 in a nitrogen stream for three different periods (10, 20, and 30 min) was used. After the regeneration step, the hydrogen yield during subsequent pyrolysis increased to 19%, 24%, and 30% for the three periods, respectively, showing that oxidation can partially be used to

recover the activity of char. However, there is not much interest in regenerating deactivated carbons, at least with the currently available techniques, because of the derived CO/CO_2 emissions and the possible consumption of the initial catalyst after many regenerations, necessitating fresh makeup catalyst [94].

The deactivation and the complexity of the regeneration of conventional catalysts used in methane cracking could provide additional motivation to investigate solar-driven methane cracking (noncatalytic). Solar concentrated energy allows operation at very high temperatures, ranging between 1000 °C and 1900 °C depending on the insolation and the concentration factor [95,96]. Theoretically, there is no need for catalysts at such high temperatures, and hence there are no issues related to deactivation and regeneration. Therefore, methane may undergo direct thermal decomposition. Moreover, solar energy utilization keeps the green aspect of the methane cracking process without any greenhouse gas emissions.

2.3. Solar Methane Pyrolysis

2.3.1. Advantages and Perspectives

Concentrated solar energy provides higher solar to heat efficiency than photovoltaic (PV) cells. PV solar to electricity efficiency (or PV solar to heat efficiency for a perfect electric heater) is in the range of 15–20% [97], while high-temperature concentrated solar thermal energy can be produced with about double the efficiency [96]. The use of concentrated solar energy for process heat has already been investigated for methane dissociation in solar reactors up to 50 kW scale [14,95,96,98–113]. However, most solar experiments concerned catalyzed and uncatalyzed methane pyrolysis in the gas phase, but not yet methane cracking in molten media. Solar energy allows for driving the pyrolysis reaction at very high temperatures (up to ≈1900 °C), thereby enhancing methane conversion. A catalyst usage is still an option to promote kinetics; however, with such harsh operating conditions, a complete conversion could be attained under the only effect of temperature at sufficiently long residence times. Thus, no catalyst deactivation and regeneration issues are encountered, and no extra cost results from their deterioration. Furthermore, solar energy completely ensures zero CO/CO_2 emissions, as the energy resource providing the heat is renewable. These advantages promoted research that aimed to study conventional pyrolysis in solar reactors, either directly or indirectly irradiated.

2.3.2. Direct vs. Indirect Heating

In solar thermochemical processes necessitating high temperatures, reactors can be implemented in two different ways to capture the solar energy. Solar reactors can be directly or indirectly heated, which chiefly differs by the way solar radiation is transferred to the reactants [114]. Figure 1 represents two types of solar reactors used in methane cracking.

In directly-irradiated solar reactors (Figure 1a), radiative heat is received through either an open aperture or a closed transparent window (e.g., quartz). Thus, reactants can be directly heated by solar radiative flux. Hydrogen production requires a windowed reactor to separate combustible products from atmospheric oxygen. Unfortunately, the contamination of a barrier window by absorptive contaminants can cause local heating and window failure. However, in such reactors, reactants can be efficiently heated by direct radiation atop conduction and convection if products and/or reactants absorb in the visible spectrum [115].

In contrast, indirectly-irradiated reactors (Figure 1b) receive solar radiations through an intermediate opaque wall, and heat is thus transferred to reactants by infrared reradiation, conduction, and convection. This type of reactor leads to higher radiative losses due to the high temperature of the absorbing wall, as compared to the reaction zone. However, a window is no longer required, and there is no issue related to window cleaning [116]. In hydrocarbon cracking, indirectly-irradiated reactors seem more suitable because the gas has a low capacity to absorb solar radiations and it must be heated mainly by conduction and convection [110,117]. To enhance the solar radiation absorption and methane conver-

sion, it is possible to feed fine particles that can sometimes play a dual role of both heat absorber and catalyst.

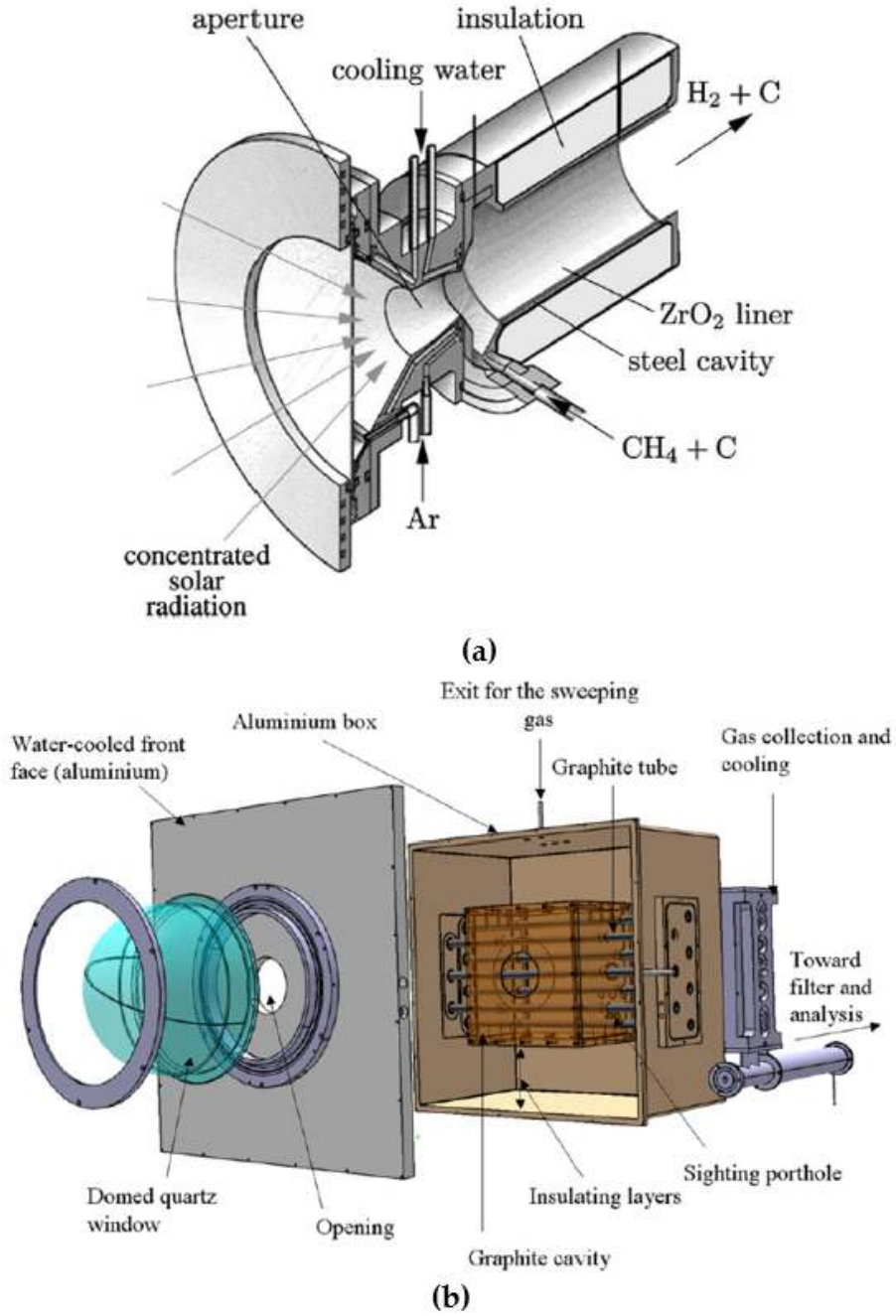

Figure 1. Directly- vs. indirectly-irradiated solar reactors used for methane pyrolysis: (**a**) 5 kW directly-irradiated reactor (Copied from Ref. [108] with Elsevier permission), (**b**) 50 kW indirectly-irradiated reactor (Copied from Ref. [102] with Elsevier permission).

2.3.3. Carbon Co-Feed

Few researchers fed carbon particles to enhance solar radiation absorption in solar methane cracking reactors (Table 1). Others investigated the catalytic activity of these carbon particles. However, it is often difficult to discriminate heat transfer enhancement from catalytic effects.

Table 1. Main studies concerning solar methane cracking in gas phase (NA: not available).

Reference	Year	Heating Mode	Catalyst	Carbon Co-Feed	T (°C)	τ_r (s)	X_{CH4} (%)
Kogan and Kogan [107]	2003	Indirect irradiation	No catalyst	None	1047	NA	27.3
Dahl et al. [95]	2004	Indirect irradiation	No catalyst	CB	1860	0.01	90
Abanades and Flamant [14]	2007	Direct irradiation	No catalyst	None	1385	0.1	97
Abanades and Flamant [112]	2008	Direct irradiation	No catalyst	None	1400	0.25	99
Abanades et al. [98]	2008	Indirect irradiation	No catalyst	None	1580	0.018	99
Rodat et al. [103]	2009	Indirect irradiation	No catalyst	None	1550	0.011	78
						0.032	100
					1700	0.011	93
					1800	0.011	100
Rodat et al. [104]	2009	Indirect irradiation	No catalyst	None	1500	0.032	98
					1470	0.012	62
						0.035	98
Maag et al. [108]	2009	Direct irradiation	No catalyst	CB	1043	<2	98.8
Rodat et al. [102]	2010	Indirect heating	No catalyst	None	1520	0.061	99
Rodat et al. [96]	2011	Indirect irradiation	No catalyst	None	1700	0.011	93
					1800		100
Yeheskel and Epstein [106]	2011	Direct irradiation	No catalyst	None	1450	NA	100
			$Fe(CO)_5$		1200		50
			$Fe(C_5H_5)_2$		800		15–20
Abanades et al. [113]	2014	Indirect irradiation	CB	None	1200	0.12	≈100
Paxman et al. [109]	2014	Indirect irradiation	No catalyst	None	1100	NA	69
Abanades et al. [110]	2015	Indirect irradiation	CB (co-feed considered as catalyst)	CB	1250	0.113	50
						0.038	15

In general, heat transfer from wall surface to gas is low [118]. Some works examined the influence of carbon black nanoparticles co-feeding with methane to enhance the heat transfer inside the reactor, thanks to radiative volumetric absorption by the particle cloud [95,108]. It was expected that carbon surface would absorb the heat from the cavity wall and would transfer it to the gas by convection.

Dahl et al. [95] used acetylene black carbons mixed with Ar to be co-fed with methane in an indirectly-heated tubular reactor. They could not report an increase in the conversion compared with operation without carbon co-feed. They attributed this result to the small size of the reactor, expecting that carbon influence on the heat transfer will be clearer in a scaled-up reactor [95,108]. Therefore, it could be promising at industrial scale. Similarly, Abanades et al. [110] introduced CB as co-feed in an indirectly-irradiated methane cracking tubular solar reactor. The purpose was also to investigate the catalytic performance of CB. They reported no significant heat transfer improvement due to the small reactor size, suggesting that a scaled-up reactor may show better results.

Maag et al. [108] demonstrated the efficiency of the carbon co-feed for heat transfer improvement. Methane flow laden with micro-sized carbon black (CB) was introduced in a directly-heated solar reactor. The increase in the particle volume fraction increased the conversion in parallel, due to enhanced radiation absorption by particles.

The catalytic performance of CB was also investigated. Abanades et al. [113] used two types of carbon blacks (SB900 and SB280) supplied by the Japanese company Asahi Carbon in an indirectly-heated packed-bed solar reactor. The CB catalyst was in the form of pellets of diameter ranges 0.25–0.5 mm, 0.5–1 mm, and 1–2 mm. At 1200 °C and a residence time of 0.12 s, the conversion was almost complete, regardless of the carbon particle size being used. They attributed the complete conversion at such a relatively low temperature to

the catalytic effect of CB. However, SB900 started to deactivate after 1500 s while SB280 deactivation started only after 2000 s. After complete deactivation, the decomposition rate reached a plateau similar to the rate of uncatalyzed cracking reaction. This confirmed the effect of CB in favoring the decomposition of methane. The activity of SB280 was lower but it deactivated more slowly. This result was also observed when comparing the activity of AC and CB and the kinetics of carbon-catalyzed methane cracking using a solar thermogravimetric reactor [110]. A smaller activity leads to less carbon formation and hence delays the encapsulation of catalyst active sites.

Another study achieved by Abanades et al. [110] investigated the effect of other CB types, with different particle size and surface area, on the decomposition of methane. SB285 (15 nm and 210 m^2/g) and SB905 (26 nm and 77 m^2/g), supplied by Asahi Carbon (Japan), were introduced as nanopowder mixed with the reactant gas. The carbon was expected to act as a catalyst. CB presence significantly decreased the production of C_2H_2, which indicates that CB improved the selectivity. However, the conversion was very slightly influenced by the carbon co-feed, compared with the process with no carbon in the reactant gas. This result was justified by the short residence time of the reactant gas in the high temperature region of the reactor.

Other catalysts were also investigated in solar pyrolysis. Yeheskel and Epstein [106] also used catalysts ($Fe(CO)_5$ and $Fe(C_5H_5)_2$) for solar methane cracking. Comparingly to [113], the conversion was only 50% at 1200 °C (Table 1). This low conversion could be attributed to the residence time (unknown) or to the weak catalytic activities of these catalysts.

Although solar energy allows reaching very high conversions without catalysts, reactor blockage by carbon deposit growing on hot surfaces may be a serious obstacle in gas phase pyrolysis. Methane cracking in a solar flame was proposed by Rodat et al. [119,120] in order to ensure a volumetric pyrolysis reaction that should avoid wall reaction and subsequent carbon deposition leading to reactor clogging. Another worthy novel technique for methane decomposition could also be cracking in molten media. Most importantly, the liquid phase allows gathering carbon particles on the surface driven by buoyancy forces, hence preventing any reactor blockage [33,121–123]. Moreover, as molten metals/salts have high specific heat capacities, this could improve heat transfer and reduce thermal losses inside the reactor to reach higher conversions [118,124]. The association of concentrated solar energy with molten media pyrolysis could also boost solar to gas heat transfer, thanks to the bubbling regime, and provide thermal inertia to stabilize the solar process. This opens the way toward a net zero CO_2 emission pyrolysis process.

3. Methane Pyrolysis in Molten Media

3.1. Concept and Principles

Molten media are an alternative solution to overcome solid carbon adhesion on the reactor walls and to avoid its possible transport as dust carried by the produced hydrogen or the unreacted methane. The other advantages include the improvement of heat transfer (and thermal inertia) owing to the high heat capacity of molten media and the enhancement of the gas residence time due to the liquid viscosity.

Methane cracking in molten media was suggested for the first time in 1931 in a US patent [29]. Briefly, iron, or any other metal, was placed in a connected two-chamber reactor and brought to its melting temperature. The hydrocarbon gas (methane) was bubbled in the melt from one side of the reactor chamber. Oxygen (present in air) was introduced from the other chamber side in the melt to oxidize the carbon produced from the gas pyrolysis. The oxidization led to heat generation that kept the metal in its liquid phase and provided the necessary enthalpy for pyrolysis (Figure 2). Another patent came to light to prevent carbon and tar-like deposition in the reactor for heavy hydrocarbons cracking [125]. This patent suggested the possibility of using small amounts of molten salts for pyrolysis. Molten salts as fine droplets (<300 μm) contributed to fine carbon particle production. Therefore, a mist of molten salt and a superheated crude oil was fed in a chamber reactor. The effluent gas was quenched to separate the salt from the gas. Other patents also exist for hydrocarbon

pyrolysis in molten media [126–128]. The reactor design could vary, but the general trend is always the same. The carbon deposition in the reactor is avoided thanks to the contact with either the molten metal or the molten salt.

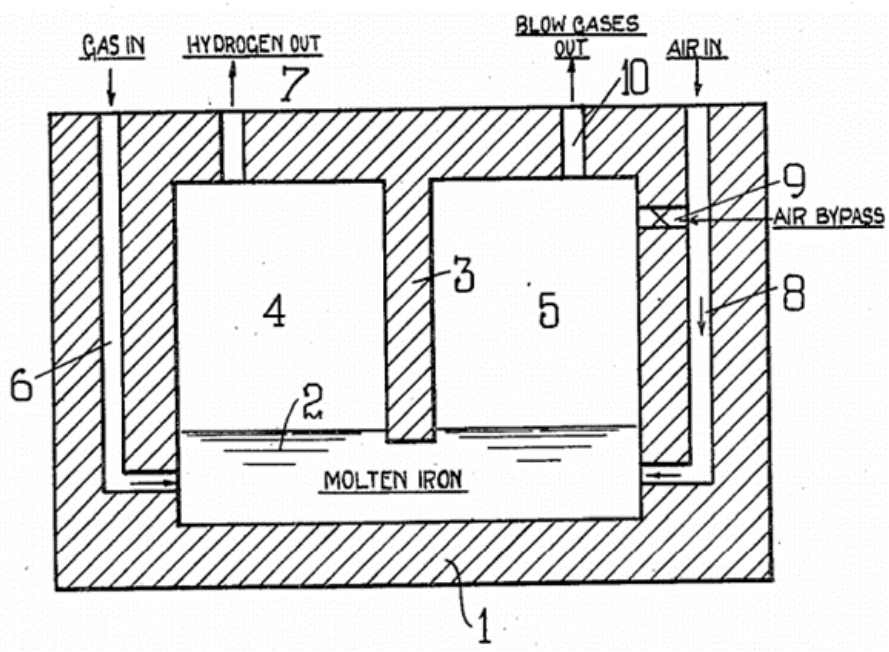

Figure 2. Two-chamber reactor design for pyrolysis in molten media from US patent of Tyrer (Copied from Ref. [29]).

3.2. Reactor Design

Figure 3 shows a conventional reactor concept for methane pyrolysis in molten media at a lab scale. This representative scheme shows an electric heater (that could be replaced by any other heat source) surrounding the walls of a reactor containing the molten medium therein. An inlet tube to feed methane is immersed in the melt so that its extremity is slightly above the bottom of the reactor. Methane is either purely introduced into the melt via the inlet tube, or mixed with other gases (Ar, H_2, etc.). A sparger can be used to split gas bubbles into smaller ones to increase the liquid–gas interface. While the bubbles rise in the melt, methane heats up and decomposes into solid carbon particles and H_2. The carbon has a significantly different density than the melt. Thus, it either floats atop, driven by buoyancy forces, or precipitates down, driven by gravity. Therefore, its collection, later on, should be theoretically feasible. The concept of such a pyrolysis reactor enables to efficiently block carbon adhesion to the reactor walls and improves the heat transfer in the reactor.

It should be noted that methane could be mixed with Ar before being introduced into the reactor [122,129]. The dilution of methane by an inert gas may help to hinder gas-phase pyrolysis before bubbling the gas in the melt. Besides, sometimes Ar is additionally fed directly into the headspace of the reactor, to guarantee negligible gas-phase pyrolysis above the melt by quenching [130,131]. This helps to avoid coke deposition on the reactor walls in the headspace, which may hinder the process continuity.

As the floating carbon should not stick to the walls of the reactor, an efficient procedure is needed to continuously remove it without stopping the process. As far as it is known to date, there is arguably no practical procedure to continuously collect and separate the floating carbon, even if it does not appear as a particular obstacle given the existing experience in metallurgy for slag removal. However, some specific attempts for carbon recovery were proposed.

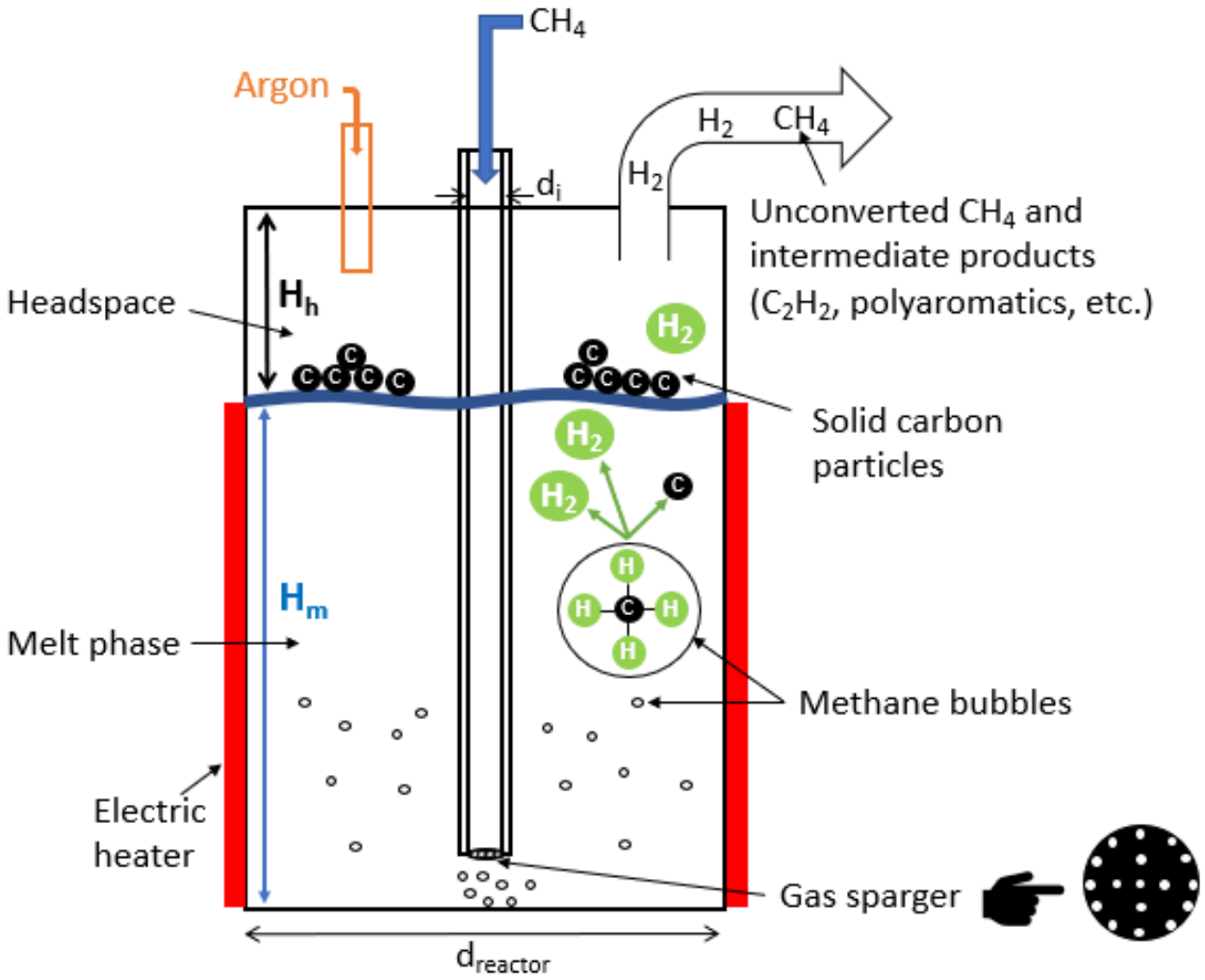

Figure 3. Representative scheme of a molten media reactor for methane pyrolysis.

Von Wald et al. [132] stated that the accumulated carbon could be removed by entrainment in the effluent gas; the carbon carried by the outlet gas flowed through a cyclone to remove the carbon particles. Then, to ensure complete carbon removal, a filter bag was placed downstream to remove very fine particles. Another design was recently suggested by Kudinov et al. [32], which could efficiently separate the carbon periodically (Figure 4). They proposed to insert in the reactor a floating structure to detect the level of the surface. When the level rises above a given threshold, the accumulated carbon quantity has to be removed. The vacuum is then turned on to collect the deposit in a small tank. Although this design seems to be promising, practical works should be performed to demonstrate its feasibility.

In the last couple of decades, several studies have been carried out to investigate methane cracking potential in molten media. Molten metals have been widely studied owing to their good catalytic activities, which are generally higher than those of molten salts.

Most experimental studies concerning methane pyrolysis in molten media are recapped in Table 2, which reports the main experimental conditions and the conversions for methane pyrolysis studies in different melts.

3.3. Molten Metals

Molten metals used for methane pyrolysis are mostly alloys of two different metals (usually, one of them is an active catalyst while the other is an inert one). Similar to solid catalysts, some molten metals are active catalysts, such as Ni, Pd, Pt, Co, and Fe [122], while others are inert or weak catalysts and show no significant catalytic effect, such as In,

Ga, Sn, Pb, and Bi [3,78,122]. While most active catalysts have high melting temperatures (>1000 °C), inert metals have much lower melting points (200–700 °C) (Table 3). Therefore, the inert metal can be the carrier or the solvent of the active metal that is expected to play the major role in catalysis.

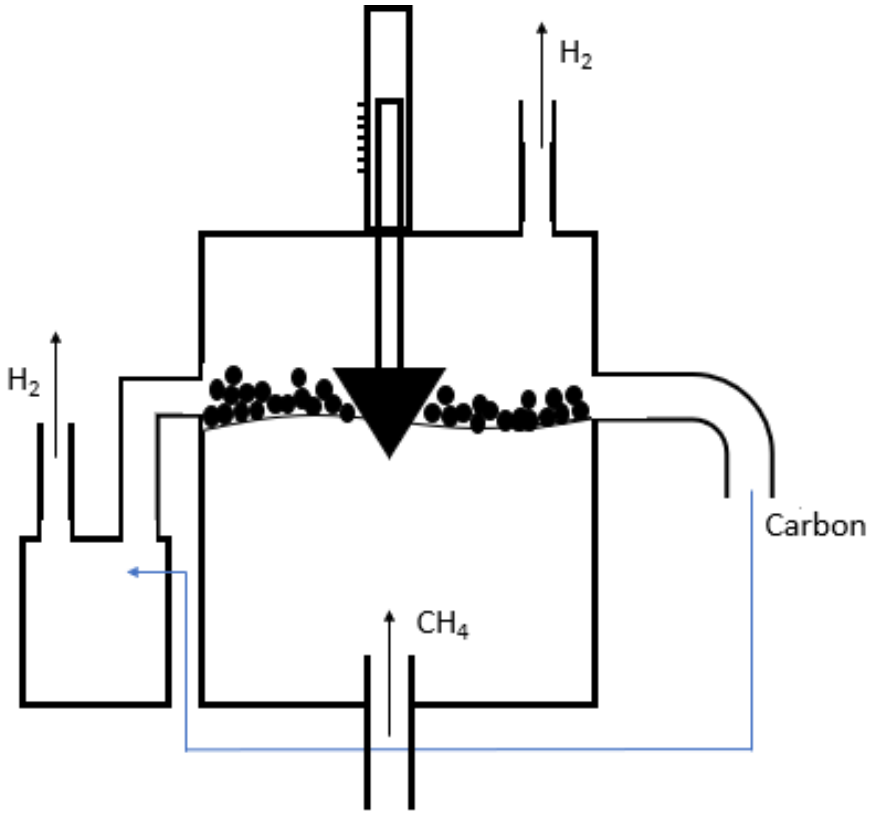

Figure 4. Reactor design for periodic carbon separation in a continuous molten media methane cracking process (adapted from Ref. [32] with Elsevier permission).

Molten media, in general, diminish the activation energy of the cracking reaction, similar to solid catalysts. The activation energies of the main molten media used for methane cracking are gathered and compared with conventional catalysts in Table 4. It can be seen that the activation energies of molten media are comparable with those of carbonaceous catalysts.

Table 2. Results of methane cracking main studies in molten media (gray: molten metals, white: molten salts, pink: two-phase molten media, green: metals suspended in molten salts).

Source	Year	Reactor Material	D (mm)	L(mm)	Filled Height (mm)	Methane Flow Rate (ml/min)	Bubble Generator Diameter	Molten Medium	Residence Time (s)	Temp (°C)	X_{CH4} (%)	X_{CH4} (%) Theoretical
Plevan et al. [3]	2015	SS	35.9	1190	600_1000	5	1 mm orifice	Tin	1.7–2.7	900	18	98
Geissler et al. [133]	2015	Quartz	40.6	1268	250 + (tin-packed bed combination (Quartz Glass, space porosity 76 vol.%, 850 mm long)	50	0.5 mm orifice	Tin	3.2–4.9	1000	32	99
Serban et al. [134]	2003	SS	25.4	355.6	101.6	15	Mott 0.5 µm porous distributor	Tin	0.3–0.5	750	51	93
Upham et al. [122]	2017	SS	30	1200	1200 (all)	10 (10% Ar)	3 mm orifice	NiBi (27:73)	≈7 s (calculated)	1065	95	99
Zeng et al. [130]	2020	Quartz	NA	70	NA	10 (43% Ar)	12 mm orifice	Te	0.5	977	22	98
Leal Pérez BJ et al. [129]	2020	NA	NA	NA	NA	450 (50% Ar)	Duran 0.2 mm porous distributor	Gallium	0.2–0.3	960–995	69–74	98–99
									0.5–0.8	936–1119	61–91	98–99
Wang et al. [123]	2008	SS	16	200	15 (calculated)	5	NA	Mg	NA	700	30	89
Parkinson et al. [135]	2021	Quartz	16	250	190	15	2 mm orifice	NaCl	0.69–0.76	1000	5.46	99
								KCl		1000	5.23	99
								NaBr		1000	4.36	99
								KBr		1000	6.22	99
								NaBr:KBr (48.7:51.3 mol%)		1000	5.85	99
Kang et al. [136]	2019	Quartz	25	250	125 (half)	20 (50% Ar)	2 mm orifice	$MnCl_2$/KCl (67:33)	0.6	1050	55 (starts at 45)	99
Kang et al. [131]	2020	Quartz	25	250	125 (half)	20 (50% Ar)	2 mm orifice	Fe (3 wt.%)/NaKCl	0.5	1000	9	99
Rahimi et al. [121]	2019	Quartz	22	300–430–1000	L-80	10 (43% Ar)	2 mm orifice	NiBi (27:73)/NaBr	4.2/1.1	1000	37.5	99
Patzschke et al. [137]	2021	Quartz	16	250	190	45 (67% Ar)	2 mm orifice	Co-Mn (molar ratio = 2) dispersed in NaBr:KBr (48.7:51.3 mol%)	NA	850–1000	10.52	98–99

Table 3. Main metal properties with calculated volumetric heat capacity (LME: London metal exchange) [138,139].

Metal	Symbol	Melting Point (°C)	Boiling Point (°C)	Density (g/cm^3) Solid vs. Liquid		LME Price (EUR/ton)	Specific Heat (J/g.°C)	ρ.Cp (J/cm^3.°C)
Tin (2 types: gray and white)	Sn	232	2602	5.77 (gray) / 7.27 (white)	6.99	25,891	0.21	1.46
Nickel	Ni	1455	2730	8.91	7.81	14,223	0.50	3.92
Cobalt	Co	1495	2900	8.90	7.75	36,957	0.42	3.24
Iron	Fe	1538	2861	7.87	6.98	422 (scrap)	0.46	3.21
Manganese	Mn	1246	2061	7.47	5.95	NA	0.48	2.84
Bismuth	Bi	271	1564	9.78	10.05	NA	0.13	1.26
Tellurium	Te	450	988	6.24	5.70	NA	0.20	1.15
Copper	Cu	1085	2562	8.96	8.02	8489	0.38	3.02
Aluminum	Al	660	2519	2.70	2.38	2006	0.92	2.19
Gallium	Ga	30	2204	5.90	6.10	NA	0.37	2.26

Table 4. Apparent activation energies for different catalysts used in methane pyrolysis reaction.

Medium	Catalyst	Apparent Activation Energy (kJ/mol)
Gas phase	Gas phase (uncatalyzed) [14–17]	356–452
	Carbon-based catalysts [14]	205–236
	Solid Ni [140]	65
	Solid Ni/SiO_2 [141]	96.1
Molten phase	Molten Fe(3 wt.%)-NaKCl: (Fe (III) introduced as $FeCl_3 \cdot 6H_2O$) [131]	171
	Molten $MnCl_2$(67%)-KCl(33%) [136]	161
	Molten Te [130]	166
	Molten Ni(67%)-Bi(33%) [122]	208
	Molten Cu(45%)-Bi(55%) [33]	222
	Molten Bi [122]	310
	Molten Tin	NA
	NaCl-KCl-NaBr-KBr [135]	231–236–278–224
	NaBr(48.7):KBr(51.3) [135]	246.7
	NaBr(48.7):KBr(51.3) [137]	236.3
	(Co-Mn)/NaBr:KBr (48.7:51.3) [137]	175.5

Although inert or weak metals exhibit low catalytic activities, their combination could highly modify the alloy activity and bring unexpected results, exceeding the performance of active metal alloys [33]. Molten metals generally having high thermal conductivities should offer isothermal conditions during pyrolysis. Thus, they could also play the role of heat transfer media to homogenize the temperature, thereby enhancing methane decomposition [33,118,129,142]. Furthermore, their high thermal capacitance may protect the process from thermal shocks due to solar energy variations in a solar methane pyrolysis process [109].

Plevan et al. [3] reported that using pure tin as a molten metal for methane pyrolysis provided no significant catalytic effect on methane conversion. This study achieved only

18% CH_4 conversion at 900 °C in a stainless-steel bubble reactor with a residence time between 1.7 and 2.7 s, which is much lower than the theoretical conversion at this temperature (98%). However, tin is known as a weak catalyst in the solid phase and, apparently, pure molten tin without being in an alloy neither enhances the catalytic activity nor the conversion [33,122].

Pure molten tin has also been investigated by Geissler et al. [133]. At a relatively higher temperature of 1000 °C and a higher residence time of 3.2–4.9 s, the conversion was 32%. Moreover, Serban et al. [134] studied methane cracking in molten tin at a much lower temperature of 750 °C, and the residence time was also shorter, counting between 0.3 and 0.5 s. In contrast, they used a 0.5 µm Mott gas sparger to increase the methane–tin surface contact. A 51% methane conversion was reached, surpassing all the results mentioned before for methane pyrolysis in molten tin. Thus, this study proved that even if tin exhibits a weak catalytic activity, the conversion can further be improved by increasing the gas–liquid interface, therefore increasing the heat transfer in the medium. This trend is expected to be true for most other molten metals since the enhanced gas–liquid interface boosts the heat transfer in the reactor.

Wang et al. [123] experimented with molten Mg as a catalyst in methane pyrolysis and reported a conversion of 30% at 700 °C in a stainless-steel reactor. This result is promising since an acceptable conversion was reached at a relatively low temperature, even without any gas spargers, which probably means that Mg has a good catalytic performance. However, the main drawback of such a molten medium is the relatively low boiling point of Mg (1090 °C) [139] and, in turn, the impossibility to operate at high temperatures to reach higher conversions [123].

Among the most recent studies concerning molten metals for methane cracking, Upham et al. [122] compared the catalytic activity of a wide variety of metal alloys using the method based on a screening reactor [122]. Briefly, this method is used to determine the catalytic activity of various catalysts. The catalyst of interest (in the form of an oxide precursor) is placed in an outer reactor and brought to its melting temperature. Then, the metal oxide is reduced by a hydrogen flow at 1000 °C. Once these steps are achieved, methane mixed with argon is flowed just over the surface of the melt so that the available contact surface is known. The effluent gas is analyzed through a mass spectrometer to determine the catalytic activity. The results of catalytic activities obtained in this study are summarized in Table 5 [122]. It was found that an alloy of $Ni_{0.17}Bi_{0.83}$ offered the highest rate of hydrogen production (9×10^{-8} mol $H_2/cm^2 \cdot s$). However, $Ni_{0.27}Bi_{0.73}$ achieved the highest conversion among all (95% in a 1.1 m column bubble reactor at 1065 °C) for an approximate residence time of 7 s. Thus, among all the tested alloys shown in Table 5, $Ni_{0.27}Bi_{0.73}$ is expected to have the best catalytic performance.

A recent study, published by Palmer et al. [33], revealed that $Cu_{0.45}Bi_{0.55}$ alloy could overcome the catalytic performance of the famous $Ni_{0.27}Bi_{0.73}$. However, such a result was not expected because Cu and Bi considered individually are both weak catalysts, while Ni is one of the most active metals investigated in methane cracking. To compare the catalytic activity of Ni–Bi and Cu–Bi alloys, they also used a screening reactor method. When comparing the turnover frequency (TOF) of both alloys at 1000 °C for different bulk concentrations, they found a slightly higher performance of $Cu_{0.45}Bi_{0.55}$ (Figure 5). They also reported a relationship between the catalytic activity and the surface concentration of the alloy: measurements of surface tension and surface composition show that Bi acts similar to a surfactant, because a small amount of added Bi substantially lowers the liquid bulk surface tension and increases the concentration of Bi at the surface. The highest TOF for Cu–Bi alloy was accompanied by the highest Bi surface concentration, which means that Bi was not inert, but it modified the properties of the bulk, and consequently enhanced the catalytic activity of the alloy. This result is interesting because Cu is 10 times cheaper than Ni, and Bi is also considered cheap.

Table 5. Comparison of liquid catalyst activity for methane pyrolysis at 1000 °C when CH_4 is flowed over 38.5 mm^2 of molten metal in a differential reactor. (*) indicates that alloy is at the solubility limit of the dissolved active metal at 950 °C.

Liquid Catalyst	Rate of Hydrogen Production (mol H_2 Produced. cm^{-2} s^{-1})
In	8.2×10^{-11}
Bi	8.2×10^{-11}
Sn	8.5×10^{-10}
Ga	3.2×10^{-9}
Pb	3.3×10^{-9}
Ag	4.3×10^{-9}
Pb vapor	2.1×10^{-9}
17% Cu–Sn *	3.1×10^{-9}
17% Pt–Sn	1.6×10^{-9}
17% Pt–Bi	4.2×10^{-9}
62% Pt–Bi *	6.5×10^{-9}
17% Ni–In	4.7×10^{-9}
17% Ni–Sn	5.6×10^{-9}
73% Ni–In *	6.4×10^{-9}
17% Ni–Ga	7.9×10^{-9}
17% Ni–Pb	8.3×10^{-9}
17% Ni–Bi	9.0×10^{-8}
27% Ni–Au *	1.2×10^{-8}
27% Ni–Bi *	1.7×10^{-8}

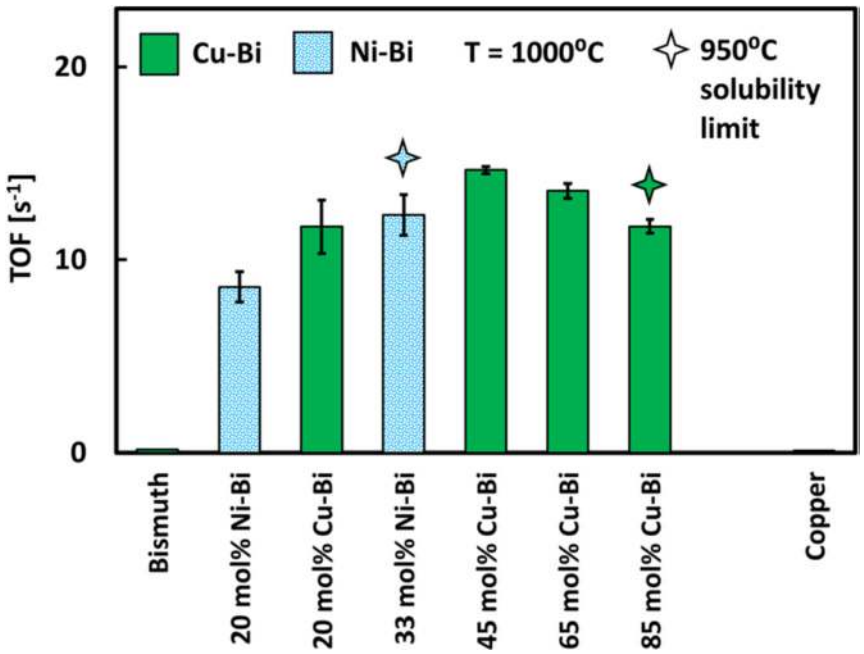

Figure 5. TOF for methane cracking over Cu–Bi, Ni–Bi alloys and pure Bi at 1000 °C. Pure copper is tested at 1100 °C (Copied from Ref. [33] with American Chemical Society permission).

Zeng et al. [130] experimentally studied the catalytic activity of pure tellurium (Te) and Ni–Te alloys to compare the catalytic activity of Te with the former best known $Ni_{0.27}Bi_{0.73}$ alloy. Pure molten Te showed a better catalytic performance than all other alloys, including $Ni_{0.27}Bi_{0.73}$ (Figure 6). They also demonstrated that Te vapor had some catalytic activity but was still significantly lower than the liquid Te phase. This was attributed to a probable relationship between the catalytic activity of Te and its affinity and electronegativity. Although these results reveal an efficient catalyst for methane pyrolysis, Te rarity and high cost are a serious barrier against process scale-up. However, such study motivates further investigation of Te-containing alloys in future works in order to discover other highly active molten media for methane cracking.

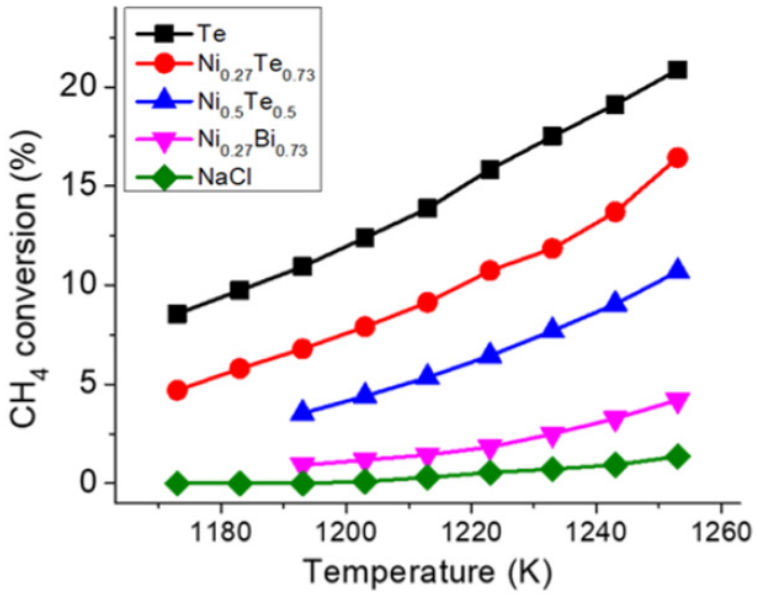

Figure 6. Methane conversion of pure Te compared with Ni–Bi and Ni–Te alloys, as well as with molten NaCl (Copied from Ref. [130] with American Chemical Society permission).

Leal Pérez et al. [129] investigated methane pyrolysis in molten gallium and obtained 91% CH_4 conversion for a residence time of 0.5 s at 1119 °C. However, Ga was reported to be a weak metal catalyst with only a slight ability to catalyze methane pyrolysis [122]. Therefore, this possible high conversion could be related to two main reasons. First, a 0.2 mm Duran gas sparger was used to split gas bubbles into smaller ones. This feature should not be underestimated, as a higher gas–liquid interface boosts the heat transfer in the medium and results in much higher conversion. In addition, the high temperature (1119 °C) could also explain, to some extent, the high conversion reached in an inert molten metal. However, gallium is very expensive, and the investigation of other cheaper metals (such as Bi, Al, Sn, etc.) is interesting to compare with gallium. Table 3 shows that Sn properties are close to that of Ga (especially the volumetric heat capacity), which encourages more investigations on Sn-containing melts because it is much cheaper than Ga.

Despite the advantages offered by molten metals in methane pyrolysis, there are some challenges to overcome. Some metals have a high vapor pressure, hence a part thereof evaporates under high temperatures. The vapor that saturates the headspace can condense in the pores of the carbon particles. As a result, the carbon may be highly contaminated, thus requiring purification for commercialization. In contrast, the purification of carbon is somehow complicated because metals cannot be easily flushed out. This complexity could be an issue for carbon storage in the case of toxic metals such as Ni and Co, or could result in economic losses in the case of expensive rare metals such as Te and Pd [121]. For example, Rahimi et al. [121] reported 83 wt.% metal contamination in the carbon for Ni–Bi molten alloy, whereas Zeng et al. [130] reported 2 atom% (0.21 wt.%) Te contamination. Some other

molten media showed low contamination, such as the 0.7 wt.% tin contamination reported by Geissler et al. [143]. As an alternative to molten metals, molten salts (eventually coupled with molten metals) have been investigated and are discussed in the following section.

3.4. Molten Salts

Molten salts as liquid media have been investigated for many centuries in metal extraction, glass manufacturing, and, recently, fused-salt electrolysis, pyrolysis of hydrocarbons including propane, and cracking of aromatic compounds [144,145]. It was also recently studied for methane cracking either as a pure salt [135,136] or coupled with a molten metal alloy [121].

The concept of molten salt reactors is similar to metal baths with some advantages over molten metals: they have a lower vapor pressure, and the salt-contaminated carbon is much easier to purify because salts are highly soluble in water [136,144]. Rahimi et al. [121] investigated methane cracking in two-phase molten Ni/Bi alloy with an upper molten salt phase of KBr or NaBr. Rahimi et al. [121] and Thomas et al. [146] stated that the salt did not only reduce the metal vapor in the headspace, but also purified the carbon byproduct from metal impurities residing in the pores of the carbon. Indeed, the presence of a salt phase above the metal phase helps to condense the metal vapor and brings it back to the molten metal phase due to density differences. A high-density difference between the salt and the metal leads to easier condensation and efficient reduction of metal losses as vapor. In the case of close densities, the metal disperses in the salt, and then bubbles completely detach from the salt interface [121].

Briefly, the effect of salt on decreasing the metal contamination of carbon was proven by Rahimi et al. [121]. Less than 5 wt.% metal contamination was reported in the case of two-phase molten media pyrolysis, compared to almost 83 wt.% metal contamination in the case of single molten Ni/Bi medium pyrolysis.

The key property for the carbon–salt separation is the wettability, defined by the Young–Dupre equation [147]. It is inversely related to the contact angle between the three-phase boundary (solid carbon interface, liquid interface, and gas interface) linked to the surface tension of the salt and the adhesion energy between the solid carbon particles and the salt. In other words, the balance between adhesive and cohesive forces defines the wettability. According to Rahimi et al. [121], NaBr and KBr have wettability values of 6 and 113 mJ/m^2, respectively, to graphene surface. This indicates that KBr had a higher wettability, and the carbon was still partially dispersed in the salt and did not float atop completely. Table 6 [121] shows a decrease of the metal content in the carbon when increasing the molten salt volume, but an increase in salt content at the same time. It can be seen that when the height of molten salt was decreased from 240 mm to 110 mm, Ni and Bi contents in the carbon increased significantly from 0.04 and 0.62 wt.% to 0.55 and 3.30 wt.%, respectively, for a water-washed procedure. It seems that adding more salt to remove metals from the carbon is efficient, but this leads to more salt contamination. However, the carbon is still easier to purify because the salt can be separated as it is highly soluble in water, unlike metals.

Table 6. XRF analysis of the solid carbon produced in the two-phase methane cracking.

Sample	C (wt.%)	Ni (wt.%)	Bi (wt.%)	K (wt.%)	Br (wt.%)
NiBi/KBr (110/240)-water washed	68.00	0.04	0.62	12.66	18.68
NiBi/KBr (240/110)-water washed	78.25	0.55	3.30	7.69	10.21

In the study of Kang et al. [136], two molten salts were used to investigate the catalytic activity of a pure molten salt pyrolysis process. KCl was considered as a weak salt catalyst, while $MnCl_2$ was a mediocre one. Therefore, they were mixed to enhance the catalytic performance. Results showed that a 67:33 mol% mixture of KCl:$MnCl_2$ had better performance than either pure KCl or pure $MnCl_2$. This result means that KCl was not an

inert solvent, but it enhanced the catalytic activity of $MnCl_2$. Moreover, the addition of $MnCl_2$ to KCl decreased the activation energy from 300 kJ/mol to ~161 kJ/mol for the same mixture. Methane conversion started at 45% and stabilized at 55% after nearly 5 h for 30 h of continuous operation without changes. This rise could be interpreted as the intermixing of the carbon byproduct with the salt to form a slurry, thereby increasing the viscosity of the medium. Therefore, this decreases the rising velocity of the bubbles in the salt, allowing for higher residence time and, consequently, higher conversions. It was also reported that when the concentration of $MnCl^{2-}$ in the solution increased, so did the catalytic activity.

Parkinson et al. [135] studied methane cracking in five different molten salts: NaBr, KBr, KCl, NaCl, and a eutectic mixture of NaBr/KBr (48.7/51.3 mol%). In a quartz reactor, at 1000 °C and a bubble residence time of 0.69–0.76 s, KBr achieved the highest conversion of 6.22%, followed by NaBr/KBr (5.85%), NaCl (5.46%), KCl (5.23%), and finally NaBr (4.36%). The low conversion could be either attributed to the low catalytic activities of these salts or to the limited heat transfer due to the generation of large bubbles (2 mm orifice). It was also found that Na-containing salts slightly wetted the carbon, while K-containing salts had higher adhesion energies. Thus, Na-containing salts yielded purer carbon materials than salts, including K.

A study of solid metals dispersed in molten media was also proposed. Patzschke et al. [137] investigated solid catalysts (metals) dispersed in molten media for the first time. They used a mixture of molten salts based on a previous study [135]. NaBr/KBr (48.7:51.3 mol%) was the molten media for methane cracking. The solid catalysts were prepared and tested through the screening procedure. A wide variety of supported catalysts were studied: La_2O_3 (10 wt.%) on Al_2O_3, NiO (10 wt.%) on Al_2O_3, NiO (10 wt.%) and La_2O_3 (10 wt.%) on Al_2O_3, Mn (5 wt.%) on Al_2O_3, MnCo (5 wt.%) on Al_2O_3, Mn (5 wt.%) on $MgAl_2O_4$, MnCo (5 wt.%) on $MgAl_2O_4$, and Co (5 wt.%) on $MgAl_2O_4$. The metals with nanocrystal sizes were prepared by colloidal chemistry. It was found that the catalysts containing Co–Mn avoided the formation of carbide and hence resulted in higher conversion rates. When the Co–Mn molar ratio was increased from 0 (Co-free) to 2, the conversion was enhanced from 4.8% to 10.4% at 1000 °C. Co–Mn-containing media showed nearly 100% hydrogen selectivity, with a stable activity over 24 h (difference < 0.5%). Generally, high Co percentage in the catalyst offered more resistance against coking and carbide formation, mainly due to the interaction between Co and Mn, which hindered the interaction with the support, forming spinel oxides such as $CoAl_2O_4$ and $MnAl_2O_4$.

These results are promising to investigate further solid catalysts in molten salts, especially those containing Co, as they efficiently prevented deactivation over continuous operation. Regarding the influence of such a process on methane conversion, further experiments should be performed, especially those involving active metals (e.g., Ni), to examine their effect on methane decomposition.

3.5. Comparison of Molten Metals and Molten Salts

Methane cracking in molten media is still a new path, not extensively investigated to date. In other words, there are no clear preferences about the most suitable media for high process efficiency (i.e., high conversion, low cost, pure carbon production, process continuity, etc.). However, based on salts and metals constellation experimented to date in molten media pyrolysis, the main differences between these two phases can be highlighted (Table 7).

Table 7. Comparison between the features of molten metals and molten salts used in methane cracking.

	Cost	**Catalytic Activity**	**Carbon Purification**	**Vapor Pressure**	**Melting Points**
Metals	High	High	Complex	High	High
Salts	Low	Moderate or low	Easy	Low	Low

Molten metals show higher performance in terms of catalytic activities [122]. Some metals are highly active in their solid state (Ni, Te, etc.), and apparently, they keep this feature when they are used in the form of melts [41–45].

Although catalysis is beneficial for methane cracking, it seems to be the only advantage of molten metals when compared with salts. Salts are indeed weaker catalysts for cracking. However, they are less expensive than metals, and less dense due to the high intermolecular interaction, thus requiring less quantity to fill the same volume filled by a metal [148]. Therefore, using molten salts may contribute to reducing the investment cost of the methane cracking process. Moreover, the carbon contaminated with salt is much easier to purify since the salt is flushable by dissolution in water. Salts have low vapor pressure, diminishing salt evaporation (this phenomenon causes carbon contamination and significant melt losses). Moreover, salts melt at a relatively lower temperature compared with metals, which reduces the energetic requirements of the process and hence increases the large-scale feasibility.

In summary, molten metals and salts require more investigations in methane pyrolysis. Carbon byproduct could be of specific interest if purified and commercialized. This may improve the process economics and, in turn, reduce hydrogen production cost to become competitive with respect to SMR. In the next section, the carbon characteristics produced from solid catalysts and molten media methane pyrolysis are discussed.

3.6. Reaction Kinetics

In the following, a review of the kinetics of methane pyrolysis is presented. In molten media, when methane bubbles rise, there are two types of reactions: (i) an uncatalyzed gas phase pyrolysis occurring in the center of the bubbles where methane is not in contact with the liquid interface, and (ii) the catalyzed pyrolysis at the interface of the bubbles where the gas is in direct contact with the liquid. For each type of reaction, forward and reverse rates can be considered.

It is generally admitted that methane cracking is a first-order reaction [3,34,146]. The forward reaction rate is a function of methane concentration:

$$r_f = k_f C_{CH4} = k_f \left(\frac{P_{CH4}}{RT} \right) \quad (8)$$

where k_f is the forward rate constant (1/s), C is the component concentration (mol/m^3), P is the partial pressure of the component (bar), R is the gas constant (8.314 J/mol.K), and T is the temperature (K).

The reverse rate is a function of hydrogen concentration:

$$r_r = k_r C_{H2}^2 = k_r \left(\frac{P_{H2}}{RT} \right)^2 \quad (9)$$

where k_r is the reverse rate constant (1/s).

The equilibrium constant is obtained as follows:

$$K_{eq} = \frac{P_{H2}^2}{P_{CH4}} \quad (10)$$

K_{eq} can be obtained when the forward and reverse rates are equal:

$$k_r = \frac{k_f \cdot (RT)}{K_{eq}} \quad (11)$$

The global reaction rate law is given by:

$$r = r_f - r_r = \frac{k_f}{RT} \left(P_{CH4} - \frac{P_{H2}^2}{K_{eq}} \right) \quad (12)$$

For simplicity, reverse reaction can be assumed negligible ($k_r = 0$), then the global rate law becomes equivalent to Equation (8).

k_f has an Arrhenius dependence with an activation energy of 391.6 kJ/mol and a pre-exponential factor of 3.8×10^{13} s^{-1} [146].

The total decomposition rate expression is the sum of gas-phase (noncatalytic) and melt-phase (catalytic) rates:

$$r_t = r_g + r_m = (k_g + k_m) \cdot C_{CH4} \quad (13)$$

Since the kinetics of uncatalyzed gas phase are known in literature, then the kinetics of the catalyzed molten phase reaction itself can be calculated by the subtraction $r_t - r_g$.

4. Carbon Product Market and Characteristics

The carbon byproduct deriving from methane decomposition has an impact on the economic feasibility of the process if a suitable carbon market is found. According to Riley et al. [149], the cost of hydrogen production can be reduced from 2.68 EUR/kg H_2 to 0 EUR/kg H_2 if all the produced carbon is sold at a price of 0.82 EUR/kg.

According to the international energy agency (IEA), the total H_2 production in 2019 was around 115 million tons. According to the stoichiometry of methane pyrolysis (Equation (3)), carbon production is three times the H_2 production in terms of weight. Therefore, if all the yearly H_2 demand is produced through methane cracking, the carbon production would be around 345 million tons, which sharply exceeds the current yearly global carbon demand (<20 million tons) [37].

Thus, industrializing methane cracking in the near future would swamp the market with unnecessary solid carbon. Hence, solid carbon sequestration and/or new carbon applications should be developed to promote the path toward a green H_2 production through methane pyrolysis.

Based on the importance of the carbon market in the economy of methane pyrolysis, it should be noticed that carbons have different selling prices depending on their types and properties. For example, carbon black has an expected price of 0.3–1.7 EUR/kg against 8 EUR/kg for graphitic carbon and 20–94 EUR/kg for carbon fibers [10]. The following section describes the carbon characteristics based on the process conditions. The type and the quality of the carbon byproduct are directly related to the operating conditions and the catalyst used in pyrolysis. Other studies report that a higher dilution ratio also affects the size of the carbon particles by yielding bigger ones [5].

4.1. Solid Metal-Catalyzed Pyrolysis

With solid metallic catalysts, there is generally formation of nanotube and nanofiber carbons. In parallel, the diameter and the length of these nanofilaments decrease with increasing temperatures, while the crystallinity increases [34].

A mechanism was proposed to understand the formation of filaments over metal-catalyzed hydrocarbons decomposition (Figure 7) [150]. Figure 7 describes the catalyst deactivation mechanism. The carbon atoms diffuse through and around a catalyst particle. Meanwhile, they form a filament until the carbon covers the entire surface, denoting complete coking. The front surface of the catalyst where the dissociation occurs should be hotter than the rear surface which is in contact with the support. Although there is no agreement about the driving force (temperature gradient or carbon concentration gradient), it is believed that carbon diffusion occurs at the peripheries of the catalyst toward the cold rear surface. This precipitation leads to carry the metal particle far away from the support, which explains the presence of an anchored metal atom at the tip of the filament (Figure 7a). The diffusion that also occurs inside the metal is the rate-determining step. This way, the filament grows until a carbon layer eventually encapsulates the surface of the catalyst and reduces the diffusion rate, leading to coking (Figure 7b). However, this mechanism does not explain the filament deviations and does not take into consideration the nature and the morphology of the catalyst particle.

Figure 7. Proposed mechanism for a carbon filament formation over a metallic catalyst: (**a**) filament formation, (**b**) coking.

Takenaka et al. [41] reported that Pd-doped Ni supported on CF results in unique nanofiber carbon structures formation. Pd/CF was also somehow similar with a Pd atom anchored at the tip but with other Pd atoms figuring in the fiber as well. However, Pd–Ni/CF resulted in branched carbon nanofibers formation, one of the rarest carbon structures yielded by methane cracking so far. In a previous study, Ni/SiO_2 also resulted in carbon nanofibers formation with a Ni atom present at the tip [151]. According to other authors [42], the coke morphology is directly related to the equilibrium between three main steps: methane activation–decomposition, carbon diffusion through the pores, and, finally, carbon precipitation or deposition. When the carbon formation surpasses the diffusion rate, there is encapsulation of the metal catalyst. Unsupported Ni led to the formation of carbon nano-onion (CNO), because of the high activation rate offered by Ni surface, leading to an excessive carbon deposition on the catalyst's surface (and gradual encapsulation). In contrast, unsupported Pt led to carbon nanotubes formation (CNT), because of the lower activation rate offered by Pt for methane decomposition. Consequently, there is much less carbon formation and hence diffusion through the pores, which delays the surface encapsulation and allows carbon nanotube formation. Ni–Pt alloy contributed to the formation of CNT, most probably because of the higher surface area that allowed more diffusion and kept the equilibrium with the dissociation and the deposition rate.

4.2. Carbon-Catalyzed Pyrolysis

In the case of carbonaceous catalysts, different types of carbons are formed with different morphologies. Savankumar et al. [24] reported the formation of carbon nanofibers and carbon nanospheres at 700 °C and 900 °C, respectively, over both biochar and activated char. However, the crystallinity of the produced carbon was higher over biochar. At higher temperatures, nanofibers were replaced by nanospheres. This could be attributed to higher methane dissociation that overloads the catalyst capacity to allow diffusion, and blocks the growth of the filaments. Methane cracking over three different CB types was reported to yield little graphite structure [23]. Different CBs showed the formation of uniform crystallite coating. One of the CBs was water- and ash-rich and resulted in uniform coating formation with small filaments identical to those seen when using metal catalysts (Ni). This was attributed to the presence of metal impurities in the carbon catalyst [79].

4.3. Pyrolysis in Molten Media

In molten media, the carbon formation was mostly different from conventional gas-phase pyrolysis over solid metals and carbons. When methane molecules decompose in the melt, C atoms are solubilized, often preventing filaments formation such as nanofibers and nanotubes. However, it is still possible to obtain such structures from pyrolysis in some melts. C atoms accumulate on the surface of the molten phase due to their lower densities, and are usually contaminated with metals or salts carried from the melt [122,131,136]. Rahimi et al. [121] reported that a single Ni–Bi phase yielded flakes of graphitic carbons, while a Ni–Bi/salt (KBr or NaBr) two-phase reaction yielded nanotube structures and carbon black aggregates. However, the predominant morphology was the sheet-like

structure. Kang et al. [131,136] also confirmed the formation of graphitic carbon in a single molten alkali halide and molten salts pyrolysis.

Consequently, it seems that salts favored the production of graphitic carbons. Molten Te led to the formation of layered carbon structure with significant disorder [130]. According to Serban et al. [134], pyrolysis in molten Sn formed graphitic carbon. Molten Mg led to the accumulation of fluffy carbon on the surface, which should be easy to separate later on [123].

5. Parameters Affecting Methane Conversion

5.1. Temperature and Pressure

As methane pyrolysis is an endothermic reaction, providing heat is essential to reach higher conversions, given that decomposition is favored when the temperature increases [3,5,18,23,24]. Figure 8 shows a thermodynamic equilibrium calculation performed using Cantera software [152] for temperatures up to 1600 °C, and for pressures ranging from 1 to 30 bar. The results confirm the expected temperature effect on the conversion. Methane starts to split into H_2 and solid carbon at 300 °C, with a complete conversion reached above 1200–1450 °C depending on the operating pressure [5]. However, in catalyzed pyrolysis, a temperature limit helps to avoid fast catalyst deactivation [13,23]. This is due to the limited pore aperture of the catalyst. Once there is high carbon formation at high temperatures, pores may be overloaded, and carbon then starts to encapsulate the surface of the catalyst, leading to deactivation. For example, Ni-based catalysts deactivate rapidly at temperatures above 600 °C [54,55,153]. In contrast, Fe-based catalysts are more resistant to deactivation with optimal performance at temperatures between 700 and 1000 °C, because methane access to the active sites is easier in the case of Fe [19,153,154]. It is generally admitted that any parameter increasing the reaction rate also fosters catalyst deactivation. Even for catalysts with more open surface area, there is always a limit where the carbon deposition on the active sites of the catalyst risks surpassing the diffusion rate through the pores, leading to deactivation [18].

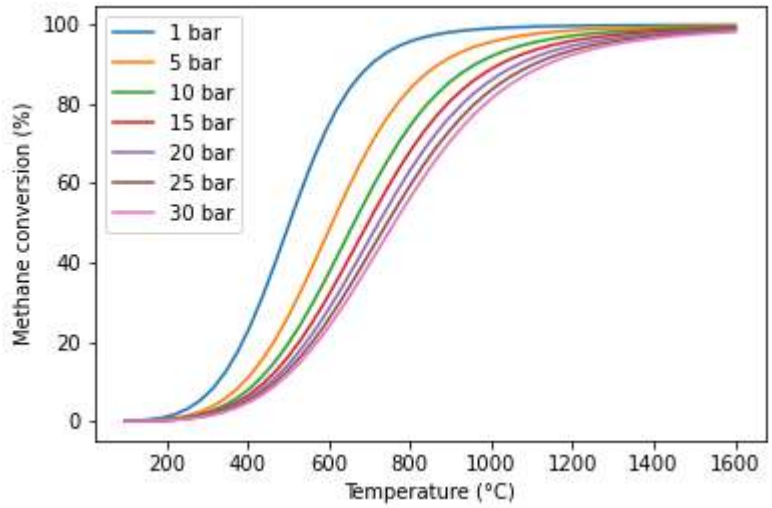

Figure 8. Equilibrium conversion of methane as a function of temperature and pressure (calculations performed with Cantera [152]).

In contrast, and based on Le Chatelier's principle, increasing the pressure shifts the reaction backward, yielding lower conversions (Figure 8) [3,155]. However, higher pressures result in higher total hydrogen yields in catalytic pyrolysis, especially at elevated temperatures [156]. This effect is directly related to the catalyst deactivation phenomenon. At atmospheric pressure, the catalyst undergoes sharp deactivation at high temperatures. In contrast, higher total pressures lead to higher partial pressure of hydrogen, which reduces catalyst deactivation.

To check this behavior, Popov et al. [156] tested the effect of temperature and pressure on methane conversion and hydrogen yield over a Ni–Cu alloy catalyst. At 600 °C, increasing the total pressure from 1 to 10 atm increased the hydrogen yield from 26 mol/g_{cat} to 40 mol/g_{cat}, and the catalyst lifetime from 17 to 40 h, but decreased the initial conversion from 37 to 20%. When the same pressure variations were applied at a higher temperature (675 °C), this behavior was more pronounced: the hydrogen yield increased by almost 10 times from 5 mol/g_{cat} to 54 mol/g_{cat} with a great increase in catalyst lifetime from 2 to 40 h, and a conversion decrease from 60 to 30%.

However, there are not many studies of high-pressure effects on methane decomposition in the literature. At industrial scale, the benefits of high pressure could be of special importance to reduce the reactor volume. Some catalysts are very expensive (e.g., Ni and Pt), and a significant lifetime extension could reduce costs, favoring the competitiveness. Pyrolysis driven at high pressures is also advantageous because it produces pressurized hydrogen, thus saving energy for compressed H_2 storage.

5.2. Feed Flow Rate

The feed gas flow rate is a critical factor influencing methane decomposition. However, the way it affects the conversion is quite different between gas-phase and molten media pyrolysis.

In gas-phase pyrolysis (catalytic or not), the inlet gas flow rate directly defines the space time of methane molecules in the reactor. A higher flow rate results in shorter spacetime. Therefore, methane molecules have less contact time to adsorb on the active sites of the catalyst, leading to relatively low conversions [23]. Moreover, it has been reported that a high flow rate may fasten the deactivation due to high carbon production rates overwhelming the carbon diffusion through the pores [23,157–159]. Thus, coking is favored at high flow rates, and early deactivation may take place. Nevertheless, high flow rates help to mix the gas and the catalyst, and improve the heat and mass transfer. Consequently, lowering the flow rate is useful to reach higher conversions with delayed catalyst deactivation, but a critical limit should be found to keep some mixing of the gas and the solid phase.

In contrast, the inlet gas flow rate in a molten medium does not significantly affect the residence time of a bubble in the liquid. The parameters that directly control this residence time are the size (diameter) of the bubble, viscosity, and melt density [131,136]. Moreover, the melt height also contributes to the bubble residence time in the molten phase since a higher height means a longer path to reach the surface. Consequently, the time a bubble needs since it detaches from the gas inlet stream to reach the surface of the melt (residence time) is independent of the flow rate itself. However, the flow rate controls the bubble formation time. A bubble slowly forms and detaches from the inlet gas stream when the inlet flow rate is low [136]. Then, the time a bubble takes to detach from the feeder could be of significant interest in the bubble heating. During its formation, the bubble is preheated by the melt, which may facilitate and hasten the methane decomposition while the bubble rises in the melt, yielding higher conversions. Nonetheless, a very low flow rate may result in early significant methane dissociation near the discharge of the gas inlet tube or the gas sparger, if used, which may induce risks of inlet reactor blockage by carbon [121,131].

To sum up, whether the inlet flow rate directly affects the gas residence time in the reactor or not, lower values should improve methane conversion in conventional methane or molten media pyrolysis. However, for molten media methane cracking, it is noteworthy not to operate at too-low flow rates, to avoid reactor blockage risks due to early gas phase pyrolysis in the inlet gas feeding tube.

5.3. Bubble Size (Molten Media)

The bubble size affects the surface contact between the gas and the melt. A higher interface leads to higher conversions because most methane molecules are in direct contact with the hot melt (possibly catalytic), which favors decomposition.

Therefore, to raise methane conversion in molten media, smaller bubbles generation is desired. The bubble size only depends on the orifice or the diameter of the methane feeding tube. Methane can be fed into the melt in two ways: either directly introduced via the inlet feeding tube, then generating relatively large bubbles, or via a gas sparger (also called a distributor) that is fixed at the discharge of the inlet feeding tube (to generate much smaller bubbles of size depending on the diameter of the sparger holes). Spargers have been used by few authors [129,134]. A clear example of the sparger effect can be evidenced when comparing the works of Serban et al. [134] with Geissler et al. [133] and Plevan et al. [3], which focused on methane cracking in molten Sn. Serban et al. [134] used a 0.5 µm Mott sparger to optimize the gas–tin interface. It is clear that even with a smaller residence time in the melt (0.3–0.5 s), methane underwent higher conversion at a much lower temperature of 750 °C (Table 2). Another study of methane cracking in molten gallium resulted in very high conversion of 91%, although gallium has always been considered as inert or a weak metal catalyst. This is most probably attributed to the 0.2 mm Duran sparger being used and to the high temperature of the melt (1119 °C) [129].

5.4. Reactor Material

In conventional gas-phase pyrolysis, the material effect on hydrocarbon decomposition has been investigated. Butane degradation over three different material reactor types, nickel, iron, and monel (Ni–Cu–Fe alloy), showed that they all had a catalytic effect on the reaction [160]. However, monel showed significantly higher influence on the catalytic performance. Monel reactor effect on olefin pyrolysis was also confirmed in another study [161]. Stainless-steel and nickel reactors showed a slight catalytic effect on the pyrolysis of propane, propylene, and ethylene cracking. In contrast, a low-carbon steel reactor had a significant influence on pyrolysis [162]. Referring to these results, the authors stated that the reactor wall surface might have some role in the initiation and the termination of the free radical formation mechanism.

However, in molten media, the methane decomposes in the melt. Thus, there is likely no significant contact between the gas and the reactor material, and hence no direct effect on catalysis. The reactor material is only in contact with the molten phase. Therefore, the reactor material should be thermally and chemically resistant under the harsh operating conditions of the process. Up to date, only quartz and stainless-steel reactors were used for methane pyrolysis in molten media (Table 3). Usually, methane cracking in molten media is driven at high temperatures (800–1200 °C), and the reactor material could face corrosion issues, especially in the case of stainless steel. In contrast, quartz is more resistant to corrosion and more mechanically stable in harsh operating conditions. Therefore, quartz is considered more suitable for methane cracking when operating at high temperatures [129].

5.5. Dilution Effect

Methane is introduced in the melt either pure or with a carrier gas: some authors introduced only pure methane [3,123,133,134], while others used methane mixed with Ar at different ratios (usually methane/Ar ratio = 1) to avoid gas phase pyrolysis in the inner methane feeding tube or even in the headspace above the melt [122,129]. Some studies also introduced Ar directly into the headspace for the same reason [130,131]. Inert Ar does not interfere in the methane reaction but acts only as a gas diluent [5]. It helps to prevent coke formation in the feeding tube or in the headspace above the melt.

However, when premixed with the feed, the Ar flow rate may modify the total flow rate of the gas. For a fixed methane flow rate, any modification in the Ar flow rate will change the total gas flow rate, and hence the methane residence time in the reactor. In contrast, if a constant flow rate is kept (only varying the mole fractions), the residence time will not be affected. Referring to Rodat et al. [105], methane conversion at 1620 °C slightly changed from 70 to 75% when the CH_4 mole fraction was tripled at a constant gas ($Ar+CH_4$) flow rate, and hence a constant residence time of 42 ms. In contrast, for fixed CH_4 and Ar mole fractions, but a doubled total flow rate, the conversion decreased from

97% to 80%, due to the residence time decrease from 50 to 25 ms. Similar results were obtained by Abanades and Flamant [112]. With a constant methane flow rate, an increase in the Ar flow rate from 0.8 NL/min to 1.2 NL/min resulted in a conversion drop from 99% to 86% due to the shorter residence time. For a constant gas flow rate, the modification of CH_4 mole fraction between 5% and 21% did not significantly affect the conversion (85% to 90%) [98].

In summary, dilution does not affect the methane conversion. However, inert gas addition can significantly modify the CH_4 conversion and the hydrogen yield when the total gas flow rate is changed, resulting in residence time variations.

6. Conclusions and Perspectives

Investigations of catalyzed methane cracking using solid metals and carbonaceous catalysts showed noticeable challenges, mainly related to catalysts deactivation and associated regeneration methods, with an overall limited efficiency and inability to conserve the green asset of methane cracking. Moreover, reactor coking could often be a problem, blocking the process continuity, controllability, and the scale-up feasibility.

To overcome the catalyst limitations, solar energy utilization could be a promising option to develop a sustainable pyrolysis process. Thanks to the high operating temperatures reachable by concentrating solar energy, thermal methane pyrolysis can be achieved, thus eliminating the need for catalysts. In addition, no CO/CO_2 emissions are derived, and the process heat for this endothermic reaction is supplied only by solar concentrated energy, thus saving fossil fuels and eliminating products' contamination by the combustion gases. However, solar reactor coking in methane pyrolysis may still need investigation. Scaling up of high-temperature solar processes also remains a challenge.

Methane pyrolysis in molten media is proven to offer important advantages over conventional pyrolysis. Carbon deposition in the reactor can be efficiently hindered, therefore enabling continuous operation. The carbon floating at the melt surface can be collected by a mechanical procedure to be treated, purified, and commercialized later. Moreover, due to the higher heat capacities of molten media compared with gases, heat transfer is improved in the reactor, which can increase the methane conversion and protect the system from thermal shocks.

Generally, although molten salts have lower catalytic activities than molten metals, they help to reduce metal vapors, and therefore metal losses, when both media are mixed together. The mix also contributes to purify the carbon from metal contamination residing in the pores. Salts are also less expensive than metals, which should enhance the economic feasibility of methane cracking and process scale-up. Some salt mixtures, such as $MnCl_2/KCl$, resulted in a good conversion (55%) at mild temperatures (1050 °C), proving that molten salts could be competitive with molten metals. Consequently, methane cracking in molten salts should garner more attention in the future.

Among the best identified metal alloys, $Ni_{0.27}Bi_{0.73}$ was confirmed as the most efficient for methane pyrolysis. However, a single recent study reported surprisingly better performance of $Cu_{0.45}Bi_{0.55}$, although Cu is catalytically weaker than Ni. Te allowed for higher methane conversions than all the Ni–Bi alloys, as well. Pure molten Ga showed also a high conversion although Ga is always reported as a weak catalyst for methane decomposition, but both high operating temperature (1119 °C) and use of a gas sparger could justify the result. Briefly, these works are promising, especially that related to Cu–Bi alloy because Cu is much cheaper than Ni. Moreover, it proves that an alloy of weak metals can further surpass the performance of an alloy containing an active metal, since an alloy can modify surface morphology.

Dispersed solid metals in molten salts showed great resistance against deactivation. Metals are known by their higher catalytic activities than salts. Therefore, coupling both metals and salts as a suspension could bring high conversions with a robust system resisting deactivation.

Metallic and carbonaceous catalysts for methane pyrolysis are limited by deactivation mechanisms. Molten media pyrolysis appears as a new path. Provided that carbon contamination can be controlled, this process could offer new perspectives either by using molten media only or by coupling molten media and solid catalysts.

Temperature, pressure, and residence time are operating parameters of primary importance. Special attention should be paid to the impact of high pressure as most of the reported works only operate near atmospheric pressure. The reacting conditions (solid catalyst, molten bath, gas-phase reaction) also affect the process and the carbon characteristics. Tuning of carbon properties according to the operating parameters is still an open research field. Finally, solar-driven methane pyrolysis in molten media has not been considered so far, while its potential has been highlighted in this review. Methane pyrolysis in new molten media solar reactors should represent a novel promising route for clean hydrogen production without CO_2 emission.

Author Contributions: Writing—original draft preparation, M.M.; writing—review and editing, M.M., S.A. and S.R.; supervision, S.A. and S.R.; project administration, S.A. and S.R.; funding acquisition, S.A. and S.R. All authors have read and agreed to the published version of the manuscript.

Funding: This work was supported by the French "Investments for the future" program managed by the National Agency for Research, under contract ANR-10-LABX-22-01 (Labex SOLSTICE).

Institutional Review Board Statement: Not applicable.

Informed Consent Statement: Not applicable.

Data Availability Statement: Not applicable.

Conflicts of Interest: The authors declare no conflict of interest.

References

1. Kothari, R.; Buddhi, D.; Sawhney, R.L. Comparison of environmental and economic aspects of various hydrogen production methods. *Renew. Sustain. Energy Rev.* **2008**, *12*, 553–563. [CrossRef]
2. Holladay, J.D.; Hu, J.; King, D.L.; Wang, Y. An overview of hydrogen production technologies. *Catal. Today* **2009**, *139*, 244–260. [CrossRef]
3. Plevan, M.; Geißler, T.; Abánades, A.; Mehravaran, K.; Rathnam, R.K.; Rubbia, C.; Salmieri, D.; Stoppel, L.; Stückrad, S.; Wetzel, T. Thermal cracking of methane in a liquid metal bubble column reactor: Experiments and kinetic analysis. *Int. J. Hydrog. Energy* **2015**, *40*, 8020–8033. [CrossRef]
4. Abánades, A. The challenge of Hydrogen production for the transition to a CO_2-free economy. *Agron. Res.* **2012**, *10*, 11–16.
5. Abánades, A.; Ruiz, E.; Ferruelo, E.M.; Hernández, F.; Cabanillas, A.; Martínez-Val, J.M.; Rubio, J.A.; López, C.; Gavela, R.; Barrera, G.; et al. Experimental analysis of direct thermal methane cracking. *Int. J. Hydrog. Energy* **2011**, *36*, 12877–12886. [CrossRef]
6. Nazir, H.; Louis, C.; Jose, S.; Prakash, J.; Muthuswamy, N.; Buan, M.E.M.; Flox, C.; Chavan, S.; Shi, X.; Kauranen, P.; et al. Is the H_2 economy realizable in the foreseeable future? Part I: H_2 production methods. *Int. J. Hydrog. Energy* **2020**, *45*, 13777–13788. [CrossRef]
7. Lemus, R.G.; Martínez Duart, J.M. Updated hydrogen production costs and parities for conventional and renewable technologies. *Int. J. Hydrog. Energy* **2010**, *35*, 3929–3936. [CrossRef]
8. Weger, L.; Abánades, A.; Butler, T. Methane cracking as a bridge technology to the hydrogen economy. *Int. J. Hydrog. Energy* **2017**, *42*, 720–731. [CrossRef]
9. Utrilla, R.; Pinilla, J.L.; Suelves, I.; Lázaro, M.J.; Moliner, R. Catalytic decomposition of methane for the simultaneous co-production of CO_2-free hydrogen and carbon nanofibre based polymers. *Fuel* **2011**, *90*, 430–432. [CrossRef]
10. Dagle, R.A.; Dagle, V.; Bearden, M.D.; Holladay, J.D.; Krause, T.R.; Ahmed, S. *An Overview of Natural Gas Conversion Technologies for Co-Production of Hydrogen and Value-Added Solid Carbon Products*; Pacific Northwest National Lab: Richland, WA, USA, 2017.
11. Muradov, N.; Smith, F.; Huang, C.; T-Raissi, A. Autothermal catalytic pyrolysis of methane as a new route to hydrogen production with reduced CO_2 emissions. *Catal. Today* **2006**, *116*, 281–288. [CrossRef]
12. Rodat, S.; Abanades, S.; Coulié, J.; Flamant, G. Kinetic modelling of methane decomposition in a tubular solar reactor. *Chem. Eng. J.* **2009**, *146*, 120–127. [CrossRef]
13. Keipi, T.; Tolvanen, K.E.S.; Tolvanen, H.; Konttinen, J. Thermo-catalytic decomposition of methane: The effect of reaction parameters on process design and the utilization possibilities of the produced carbon. *Energy Convers. Manag.* **2016**, *126*, 923–934. [CrossRef]
14. Abanades, S.; Flamant, G. Experimental study and modeling of a high-temperature solar chemical reactor for hydrogen production from methane cracking. *Int. J. Hydrog. Energy* **2007**, *32*, 1508–1515. [CrossRef]

15. Sajid, M.U.; Bicer, Y. Thermodynamic assessment of chemical looping combustion and solar thermal methane cracking-based integrated system for green ammonia production. *Therm. Sci. Eng. Prog.* **2020**, *19*, 100588. [CrossRef]
16. Gonzalez-Aguilar, J.; Dème, I.; Fulcheri, L.; Flamant, G.; Gruenberger, T.M.; Ravary, B. Comparison of simple particle-radiation coupling models applied on a plasma black process. *Plasma Chem. Plasma Process.* **2004**, *24*, 603–623. [CrossRef]
17. Holmen, A.; Olsvik, O.; Rokstad, O.A. Pyrolysis of natural gas: Chemistry and process concepts. *Fuel Process. Technol.* **1995**, *42*, 249–267. [CrossRef]
18. Abánades, A.; Rubbia, C.; Salmieri, D. Technological challenges for industrial development of hydrogen production based on methane cracking. *Energy* **2012**, *46*, 359–363. [CrossRef]
19. Ashik, U.P.M.; Wan Daud, W.M.A.; Abbas, H.F. Production of greenhouse gas free hydrogen by thermocatalytic decomposition of methane—A review. *Renew. Sustain. Energy Rev.* **2015**, *44*, 221–256. [CrossRef]
20. Pudukudy, M.; Yaakob, Z.; Jia, Q.; Sobri Takriff, M. Catalytic decomposition of undiluted methane into hydrogen and carbon nanotubes over Pt promoted Ni/CeO_2 catalysts. *New J. Chem.* **2018**, *42*, 14843–14856. [CrossRef]
21. Kopp, M.; Coleman, D.; Stiller, C.; Scheffer, K.; Aichinger, J.; Scheppat, B. Energiepark Mainz: Technical and economic analysis of the worldwide largest Power-to-Gas plant with PEM electrolysis. *Int. J. Hydrog. Energy* **2017**, *42*, 13311–13320. [CrossRef]
22. Ayillath Kutteri, D.; Wang, I.W.; Samanta, A.; Li, L.; Hu, J. Methane decomposition to tip and base grown carbon nanotubes and COx-free H_2 over mono- and bimetallic 3d transition metal catalysts. *Catal. Sci. Technol.* **2018**, *8*, 858–869. [CrossRef]
23. Dunker, A.M.; Kumar, S.; Mulawa, P.A. Production of hydrogen by thermal decomposition of methane in a fluidized-bed reactor—Effects of catalyst, temperature, and residence time. *Int. J. Hydrog. Energy* **2006**, *31*, 473–484. [CrossRef]
24. Patel, S.; Kundu, S.; Halder, P.; Marzbali, M.H.; Chiang, K.; Surapaneni, A.; Shah, K. Production of hydrogen by catalytic methane decomposition using biochar and activated char produced from biosolids pyrolysis. *Int. J. Hydrog. Energy* **2020**, *45*, 29978–29992. [CrossRef]
25. Abbas, H.F.; Daud, W.M.A.W. Influence of reactor material and activated carbon on the thermocatalytic decomposition of methane for hydrogen production. *Appl. Catal. A Gen.* **2010**, *388*, 232–239. [CrossRef]
26. Botas, J.A.; Serrano, D.P.; Guil-López, R.; Pizarro, P.; Gómez, G. Methane catalytic decomposition over ordered mesoporous carbons: A promising route for hydrogen production. *Int. J. Hydrog. Energy* **2010**, *35*, 9788–9794. [CrossRef]
27. Bai, Z.; Chen, H.; Li, W.; Li, B. Hydrogen production by methane decomposition over coal char. *Int. J. Hydrog. Energy* **2006**, *31*, 899–905. [CrossRef]
28. Abánades, A.; Rubbia, C.; Salmieri, D. Thermal cracking of methane into Hydrogen for a CO_2-free utilization of natural gas. *Int. J. Hydrog. Energy* **2013**, *38*, 8491–8496. [CrossRef]
29. Tyrer, D. Production of Hydrogen. U.S. Patent 1,803,221, 28 April 1931.
30. Steinberg, M. Fossil fuel decarbonization technology for mitigating global warming. *Int. J. Hydrog. Energy* **1999**, *24*, 771–777. [CrossRef]
31. Schultz, I.; Agar, D.W. Decarbonisation of fossil energy via methane pyrolysis using two reactor concepts: Fluid wall flow reactor and molten metal capillary reactor. *Int. J. Hydrog. Energy* **2015**, *40*, 11422–11427. [CrossRef]
32. Kudinov, I.V.; Pimenov, A.A.; Kryukov, Y.A.; Mikheeva, G.V. A theoretical and experimental study on hydrodynamics, heat exchange and diffusion during methane pyrolysis in a layer of molten tin. *Int. J. Hydrog. Energy* **2021**. [CrossRef]
33. Palmer, C.; Tarazkar, M.; Kristoffersen, H.H.; Gelinas, J.; Gordon, M.J.; McFarland, E.W.; Metiu, H. Methane Pyrolysis with a Molten Cu-Bi Alloy Catalyst. *ACS Catal.* **2019**, *9*, 8337–8345. [CrossRef]
34. Sánchez-Bastardo, N.; Schlögl, R.; Ruland, H. Methane Pyrolysis for CO_2-Free H_2 Production: A Green Process to Overcome Renewable Energies Unsteadiness. *Chem. Ing. Tech.* **2020**, *92*, 1596–1609. [CrossRef]
35. Amin, A.M.; Croiset, E.; Epling, W. Review of methane catalytic cracking for hydrogen production. *Int. J. Hydrog. Energy* **2011**, *36*, 2904–2935. [CrossRef]
36. Schneider, S.; Bajohr, S.; Graf, F.; Kolb, T. State of the Art of Hydrogen Production via Pyrolysis of Natural Gas. *ChemBioEng Rev.* **2020**, *92*, 1023–1032. [CrossRef]
37. Muradov, N.; Veziroglu, T. "Green" path from fossil-based to hydrogen economy: An overview of carbon-neutral technologies. *Int. J. Hydrog. Energy* **2008**, *33*, 6804–6839. [CrossRef]
38. Abbas, H.F.; Wan Daud, W.M.A. Hydrogen production by methane decomposition: A review. *Int. J. Hydrog. Energy* **2010**, *35*, 1160–1190. [CrossRef]
39. Samanta, S.K.; Verma, P. Advanced Hydrogen Production through Methane Cracking: A Review. *Sci. Technol.* **2015**, *1*, 109–123.
40. Chen, L.; Qi, Z.; Zhang, S.; Su, J.; Somorjai, G.A. Catalytic Hydrogen Production from Methane: A Review on Recent Progress and Prospect. *Catalysts* **2020**, *10*, 858. [CrossRef]
41. Takenaka, S.; Shigeta, Y.; Tanabe, E.; Otsuka, K. Methane decomposition into hydrogen and carbon nanofibers over supported Pd-Ni catalysts. *J. Catal.* **2003**, *220*, 468–477. [CrossRef]
42. Zhou, L.; Basset, J.M. Unsupported NiPt alloy metal catalysts prepared by water-in-oil (W/O) microemulsion method for methane cracking. *Fuel* **2016**, *181*, 805–810. [CrossRef]
43. Mei, I.L.S.; Lock, S.S.M.; Vo, D.V.N.; Abdullah, B. Thermo-catalytic methane decomposition for hydrogen production: Effect of palladium promoter on Ni-based catalysts. *Bull. Chem. React. Eng. Catal.* **2016**, *11*, 191–199. [CrossRef]
44. Ouyang, M.; Boldrin, P.; Maher, R.C.; Chen, X.; Liu, X.; Cohen, L.F.; Brandon, N.P. A mechanistic study of the interactions between methane and nickel supported on doped ceria. *Appl. Catal. B Environ.* **2019**, *248*, 332–340. [CrossRef]

45. Chen, J.; Li, Y.; Li, Z.; Zhang, X. Production of COx-free hydrogen and nanocarbon by direct decomposition of undiluted methane on Ni-Cu-alumina catalysts. *Appl. Catal. A Gen.* **2004**, *269*, 179–186. [CrossRef]
46. Ermakova, M.A.; Ermakov, D.Y.; Kuvshinov, G.G. Effective catalysts for direct cracking of methane to produce hydrogen and filamentous carbon. Part I. Nickel catalysts. *Appl. Catal. A Gen.* **2000**, *201*, 61–70. [CrossRef]
47. Bayat, N.; Rezaei, M.; Meshkani, F. Methane decomposition over Ni-Fe/Al_2O_3 catalysts for production of COx-free hydrogen and carbon nanofiber. *Int. J. Hydrog. Energy* **2016**, *41*, 1574–1584. [CrossRef]
48. Wang, D.; Zhang, J.; Sun, J.; Gao, W.; Cui, Y. Effect of metal additives on the catalytic performance of Ni/Al_2O_3 catalyst in thermocatalytic decomposition of methane. *Int. J. Hydrog. Energy* **2019**, *44*, 7205–7215. [CrossRef]
49. Bayat, N.; Rezaei, M.; Meshkani, F. COx-free hydrogen and carbon nanofibers production by methane decomposition over nickel-alumina catalysts. *Korean J. Chem. Eng.* **2016**, *33*, 490–499. [CrossRef]
50. Bayat, N.; Rezaei, M.; Meshkani, F. Methane dissociation to COx-free hydrogen and carbon nanofiber over Ni-Cu/Al_2O_3 catalysts. *Fuel* **2017**, *195*, 88–96. [CrossRef]
51. Bayat, N.; Rezaei, M.; Meshkani, F. Hydrogen and carbon nanofibers synthesis by methane decomposition over Ni-Pd/Al_2O_3 catalyst. *Int. J. Hydrog. Energy* **2016**, *41*, 5494–5503. [CrossRef]
52. Rastegarpanah, A.; Rezaei, M.; Meshkani, F.; Zhang, K.; Zhao, X.; Pei, W.; Liu, Y.; Deng, J.; Arandiyan, H.; Dai, H. Mesoporous Ni/MeOx (Me = Al, Mg, Ti, and Si): Highly efficient catalysts in the decomposition of methane for hydrogen production. *Appl. Surf. Sci.* **2019**, *478*, 581–593. [CrossRef]
53. Hasnan, N.S.N.; Timmiati, S.N.; Lim, K.L.; Yaakob, Z.; Kamaruddin, N.H.N.; Teh, L.P. Recent developments in methane decomposition over heterogeneous catalysts: An overview. *Mater. Renew. Sustain. Energy* **2020**, *9*, 1–18. [CrossRef]
54. Al-Fatesh, A.S.; Fakeeha, A.H.; Ibrahim, A.A.; Khan, W.U.; Atia, H.; Eckelt, R.; Seshan, K.; Chowdhury, B. Decomposition of methane over alumina supported Fe and Ni–Fe bimetallic catalyst: Effect of preparation procedure and calcination temperature. *J. Saudi Chem. Soc.* **2018**, *22*, 239–247. [CrossRef]
55. Berndt, F.M.; Perez-Lopez, O.W. Catalytic decomposition of methane over Ni/SiO_2: Influence of Cu addition. *React. Kinet. Mech. Catal.* **2017**, *120*, 181–193. [CrossRef]
56. Li, J.; Zhao, L.; He, J.; Dong, L.; Xiong, L.; Du, Y.; Yang, Y.; Wang, H.; Peng, S. Methane decomposition over high-loaded Ni-Cu-SiO_2 catalysts. *Fusion Eng. Des.* **2016**, *113*, 279–287. [CrossRef]
57. Echegoyen, Y.; Suelves, I.; Lázaro, M.J.; Moliner, R.; Palacios, J.M. Hydrogen production by thermocatalytic decomposition of methane over Ni-Al and Ni-Cu-Al catalysts: Effect of calcination temperature. *J. Power Sources* **2007**, *169*, 150–157. [CrossRef]
58. Zhou, L.; Enakonda, L.R.; Saih, Y.; Loptain, S.; Gary, D.; Del-Gallo, P.; Basset, J.M. Catalytic Methane Decomposition over Fe-Al_2O_3. *ChemSusChem* **2016**, *9*, 1243–1248. [CrossRef] [PubMed]
59. Wang, J.; Jin, L.; Li, Y.; Hu, H. Preparation of fe-doped carbon catalyst for methane decomposition to hydrogen. *Ind. Eng. Chem. Res.* **2017**, *56*, 11021–11027. [CrossRef]
60. Pudukudy, M.; Yaakob, Z.; Mazuki, M.Z.; Takriff, M.S.; Jahaya, S.S. One-pot sol-gel synthesis of MgO nanoparticles supported nickel and iron catalysts for undiluted methane decomposition into COx free hydrogen and nanocarbon. *Appl. Catal. B Environ.* **2017**, *218*, 298–316. [CrossRef]
61. Zhang, T.; Amiridis, M.D. Hydrogen production via the direct cracking of methane over silica-supported nickel catalysts. *Appl. Catal. A Gen.* **1998**, *167*, 161–172. [CrossRef]
62. Amin, A.M.; Croiset, E.; Constantinou, C.; Epling, W. Methane cracking using Ni supported on porous and non-porous alumina catalysts. *Int. J. Hydrog. Energy* **2012**, *37*, 9038–9048. [CrossRef]
63. Venugopal, A.; Naveen Kumar, S.; Ashok, J.; Hari Prasad, D.; Durga Kumari, V.; Prasad, K.; Subrahmanyam, M. Hydrogen production by catalytic decomposition of methane over Ni/SiO_2. *Int. J. Hydrog. Energy* **2007**, *32*, 1782–1788. [CrossRef]
64. Gac, W.; Denis, A.; Borowiecki, T.; Kępiński, L. Methane decomposition over Ni–MgO–Al_2O_3 catalysts. *Appl. Catal. A Gen.* **2009**, *357*, 236–243. [CrossRef]
65. Ermakova, M.A.; Ermakov, D.Y. Ni/SiO_2 and Fe/SiO_2 catalysts for production of hydrogen and filamentous carbon via methane decomposition. *Catal. Today* **2002**, *77*, 225–235. [CrossRef]
66. Li, Y.; Chen, J.; Chang, L. Catalytic growth of carbon fibers from methane on a nickel-alumina composite catalyst prepared from Feitknecht compound precursor. *Appl. Catal. A Gen.* **1997**, *163*, 45–57. [CrossRef]
67. Figueiredo, J.L.; Órfão, J.J.M.; Cunha, A.F. Hydrogen production via methane decomposition on Raney-type catalysts. *Int. J. Hydrog. Energy* **2010**, *35*, 9795–9800. [CrossRef]
68. Forzatti, P.; Lietti, L. Catalyst deactivation. *Catal. today* **1999**, *52*, 165–181. [CrossRef]
69. Bartholomew, C.H. Mechanisms of catalyst deactivation. *Chem. Eng. J.* **2001**, *212*, 17–60. [CrossRef]
70. Argyle, M.; Bartholomew, C. Heterogeneous Catalyst Deactivation and Regeneration: A Review. *Catalysts* **2015**, *5*, 145–269. [CrossRef]
71. Baker, R.T.K.; Barber, M.A.; Harris, P.S.; Feates, F.S.; Waite, R.J. Nucleation and growth of carbon deposits from the nickel catalyzed decomposition of acetylene. *Appl. Catal. A Gen.* **1972**, *26*, 51–62. [CrossRef]
72. Ginsburg, J.M.; Piña, J.; El Solh, T.; De Lasa, H.I. Coke formation over a nickel catalyst under methane dry reforming conditions: Thermodynamic and kinetic models. *Ind. Eng. Chem. Res.* **2005**, *44*, 4846–4854. [CrossRef]
73. Wagman, D.D.; Kilpatrick, J.E.; Taylor, W.J.; Pitzer, K.S.; Rossini, F.D. Heats, free energies, and equilibrium constants of some reactions involving O_2, H_2, H_2O, C, CO, CO_2, and CH_4. *J. Res. Natl. Bur. Stand* **1945**, *34*, 143. [CrossRef]

74. Otsuka, K.; Takenaka, S.; Ohtsuki, H. Production of pure hydrogen by cyclic decomposition of methane and oxidative elimination of carbon nanofibers on supported-Ni-based catalysts. *Appl. Catal. A Gen.* **2004**, *273*, 113–124. [CrossRef]
75. Rahman, M.S.; Croiset, E.; Hudgins, R.R. Catalytic decomposition of methane for hydrogen production. *Top. Catal.* **2006**, *37*, 137–145. [CrossRef]
76. Villacampa, J.I.; Royo, C.; Romeo, E.; Montoya, J.A.; Del Angel, P.; Monzón, A. Catalytic decomposition of methane over Ni-Al_2O_3 coprecipitated catalysts Reaction and regeneration studies. *Appl. Catal. A Gen.* **2003**, *252*, 363–383. [CrossRef]
77. Koç, R.; Alper, E.; Croiset, E.; Elkamel, A. Partial regeneration of Ni-based catalysts for hydrogen production via methane cracking. *Turkish J. Chem.* **2008**, *32*, 157–168.
78. Aiello, R.; Fiscus, J.E.; Zur Loye, H.C.; Amiridis, M.D. Hydrogen production via the direct cracking of methane over Ni/SiO_2: Catalyst deactivation and regeneration. *Appl. Catal. A Gen.* **2000**, *192*, 227–234. [CrossRef]
79. Suelves, I.; Lázaro, M.J.; Moliner, R.; Pinilla, J.L.; Cubero, H. Hydrogen production by methane decarbonization: Carbonaceous catalysts. *Int. J. Hydrog. Energy* **2007**, *32*, 3320–3326. [CrossRef]
80. Muradov, N.; Smith, F.; T-Raissi, A. Catalytic activity of carbons for methane decomposition reaction. *Catal. Today* **2005**, *102–103*, 225–233. [CrossRef]
81. Zhang, J.; Li, X.; Xie, W.; Hao, Q.; Chen, H.; Ma, X. K_2CO_3-promoted methane pyrolysis on nickel/coal-char hybrids. *J. Anal. Appl. Pyrolysis* **2018**, *136*, 53–61. [CrossRef]
82. Pinilla, J.L.; Torres, D.; Lázaro, M.J.; Suelves, I.; Moliner, R.; Cañadas, I.; Rodríguez, J.; Vidal, A.; Martínez, D. Metallic and carbonaceous-based catalysts performance in the solar catalytic decomposition of methane for hydrogen and carbon production. *Int. J. Hydrog. Energy* **2012**, *37*, 9645–9655. [CrossRef]
83. Strelko, V.; Malik, D.; Streat, M. Characterisation of the surface of oxidised carbon adsorbents. *Carbon N. Y.* **2002**, *40*, 95–104. [CrossRef]
84. Serrano, D.P.; Botas, J.A.; Guil-Lopez, R. H_2 production from methane pyrolysis over commercial carbon catalysts: Kinetic and deactivation study. *Int. J. Hydrog. Energy* **2009**, *34*, 4488–4494. [CrossRef]
85. Jung, J.U.; Nam, W.; Yoon, K.J.; Han, G.Y. Hydrogen production by catalytic decomposition of methane over carbon catalysts in a fluidized bed. *Korean J. Chem. Eng.* **2007**, *24*, 674–678. [CrossRef]
86. Lee, S.Y.; Ryu, B.H.; Han, G.Y.; Lee, T.J.; Yoon, K.J. Catalytic characteristics of specialty carbon blacks in decomposition of methane for hydrogen production. *Carbon N. Y.* **2008**, *46*, 1978–1986. [CrossRef]
87. Kim, M.H.; Lee, E.K.; Jun, J.H.; Han, G.Y.; Kong, S.J.; Lee, B.K.; Lee, T.J.; Yoon, K.J. Hydrogen production by catalytic decomposition of methane over activated carbons: Deactivation study. *Korean J. Chem. Eng.* **2003**, *20*, 835–839. [CrossRef]
88. Lázaro, M.J.; Pinilla, J.L.; Suelves, I.; Moliner, R. Study of the deactivation mechanism of carbon blacks used in methane decomposition. *Int. J. Hydrog. Energy* **2008**, *33*, 4104–4111. [CrossRef]
89. Ashok, J.; Kumar, S.N.; Venugopal, A.; Kumari, V.D.; Tripathi, S.; Subrahmanyam, M. COx free hydrogen by methane decomposition over activated carbons. *Catal. Commun.* **2008**, *9*, 164–169. [CrossRef]
90. Lee, K.K.; Han, G.Y.; Yoon, K.J.; Lee, B.K. Thermocatalytic hydrogen production from the methane in a fluidized bed with activated carbon catalyst. *Catal. Today* **2004**, *93–95*, 81–86. [CrossRef]
91. Krzyzyński, S.; Kozłowski, M. Activated carbons as catalysts for hydrogen production via methane decomposition. *Int. J. Hydrog. Energy* **2008**, *33*, 6172–6177. [CrossRef]
92. Abbas, H.F.; Daud, W.M.A.W. Thermocatalytic decomposition of methane for hydrogen production using activated carbon catalyst: Regeneration and characterization studies. *Int. J. Hydrog. Energy* **2009**, *34*, 8034–8045. [CrossRef]
93. Sun, Z.Q.; Wu, J.H.; Haghighi, M.; Bromly, J.; Ng, E.; Wee, H.L.; Wang, Y.; Zhang, D.K. Methane cracking over a bituminous coal char. *Energy Fuels* **2007**, *21*, 1601–1605. [CrossRef]
94. Yang, L.; Liu, F.; Liu, Y.; Quan, W.; He, J. Deep regeneration of activated carbon catalyst and autothermal analysis for chemical looping methane thermo-catalytic decomposition process. *Int. J. Hydrog. Energy* **2018**, *43*, 17633–17642. [CrossRef]
95. Dahl, J.K.; Buechler, K.J.; Weimer, A.W.; Lewandowski, A.; Bingham, C. Solar-thermal dissociation of methane in a fluid-wall aerosol flow reactor. *Int. J. Hydrog. Energy* **2004**, *29*, 725–736. [CrossRef]
96. Rodat, S.; Abanades, S.; Flamant, G. Co-production of hydrogen and carbon black from solar thermal methane splitting in a tubular reactor prototype. *Sol. Energy* **2011**, *85*, 645–652. [CrossRef]
97. Kumar, L.; Hasanuzzaman, M.; Rahim, N.A. Global advancement of solar thermal energy technologies for industrial process heat and its future prospects: A review. *Energy Convers. Manag.* **2019**, *195*, 885–908. [CrossRef]
98. Abanades, S.; Tescari, S.; Rodat, S.; Flamant, G. Natural gas pyrolysis in double-walled reactor tubes using thermal plasma or concentrated solar radiation as external heating source. *J. Nat. Gas Chem.* **2009**, *18*, 1–8. [CrossRef]
99. Rodat, S.; Abanades, S.; Grivei, E.; Patrianakos, G.; Zygogianni, A.; Konstandopoulos, A.G.; Flamant, G. Characterisation of carbon blacks produced by solar thermal dissociation of methane. *Carbon* **2011**, *49*, 3084–3091. [CrossRef]
100. Abanades, S.; Kimura, H.; Otsuka, H. Hydrogen production from CO_2-free thermal decomposition of methane: Design and on-sun testing of a tube-type solar thermochemical reactor. *Fuel Process. Technol.* **2014**, *122*, 153–162. [CrossRef]
101. Abanades, S.; Flamant, G. High-temperature solar chemical reactors for hydrogen production from natural gas cracking. *Chem. Eng. Commun.* **2008**, *195*, 1159–1175. [CrossRef]
102. Rodat, S.; Abanades, S.; Sans, J.-L.; Flamant, G. A pilot-scale solar reactor for the production of hydrogen and carbon black from methane splitting. *Int. J. Hydrog. Energy* **2010**, *35*, 7748–7758. [CrossRef]

103. Rodat, S.; Abanades, S.; Flamant, G. High-Temperature Solar Methane Dissociation in a Multitubular Cavity-Type Reactor in the Temperature Range 1823–2073 K. *Energy Fuels* **2009**, *23*, 2666–2674. [CrossRef]
104. Rodat, S.; Abanades, S.; Sans, J.-L.; Flamant, G. Hydrogen production from solar thermal dissociation of natural gas: Development of a 10kW solar chemical reactor prototype. *Sol. Energy* **2009**, *83*, 1599–1610. [CrossRef]
105. Rodat, S.; Abanades, S.; Flamant, G. Experimental evaluation of indirect heating tubular reactors for solar methane pyrolysis. *Int. J. Chem. React. Eng.* **2010**, *8*. [CrossRef]
106. Yeheskel, J.; Epstein, M. Thermolysis of methane in a solar reactor for mass-production of hydrogen and carbon nano-materials. *Carbon N. Y.* **2011**, *49*, 4695–4703. [CrossRef]
107. Kogan, M.; Kogan, A. Production of hydrogen and carbon by solar thermal methane splitting. I. The unseeded reactor. *Int. J. Hydrog. Energy* **2003**, *28*, 1187–1198. [CrossRef]
108. Maag, G.; Zanganeh, G.; Steinfeld, A. Solar thermal cracking of methane in a particle-flow reactor for the co-production of hydrogen and carbon. *Int. J. Hydrog. Energy* **2009**, *34*, 7676–7685. [CrossRef]
109. Paxman, D.; Trottier, S.; Nikoo, M.; Secanell, M.; Ordorica-Garcia, G. Initial experimental and theoretical investigation of solar molten media methane cracking for hydrogen production. *Energy Procedia* **2014**, *49*, 2027–2036. [CrossRef]
110. Abanades, S.; Kimura, H.; Otsuka, H. A drop-tube particle-entrained flow solar reactor applied to thermal methane splitting for hydrogen production. *Fuel* **2015**, *153*, 56–66. [CrossRef]
111. Abanades, S.; Kimura, H.; Otsuka, H. Kinetic investigation of carbon-catalyzed methane decomposition in a thermogravimetric solar reactor. *Int. J. Hydrog. Energy* **2015**, *40*, 10744–10755. [CrossRef]
112. Abanades, S.; Flamant, G. Hydrogen production from solar thermal dissociation of methane in a high-temperature fluid-wall chemical reactor. *Chem. Eng. Process. Process Intensif.* **2008**, *47*, 490–498. [CrossRef]
113. Abanades, S.; Kimura, H.; Otsuka, H. Hydrogen production from thermo-catalytic decomposition of methane using carbon black catalysts in an indirectly-irradiated tubular packed-bed solar reactor. *Int. J. Hydrog. Energy* **2014**, *39*, 18770–18783. [CrossRef]
114. Diver, R.B. Receiver/Reactor Concepts for Thermochemical Transport of Solar Energy. *J. Sol. Energy Eng.* **1987**, *109*, 199–204. [CrossRef]
115. Zsembinszki, G.; Solé, A.; Barreneche, C.; Prieto, C.; Fernández, A.; Cabeza, L. Review of Reactors with Potential Use in Thermochemical Energy Storage in Concentrated Solar Power Plants. *Energies* **2018**, *11*, 2358. [CrossRef]
116. Koepf, E.; Alxneit, I.; Wieckert, C.; Meier, A. A review of high temperature solar driven reactor technology: 25 years of experience in research and development at the Paul Scherrer Institute. *Appl. Energy* **2017**, *188*, 620–651. [CrossRef]
117. Alonso, E.; Romero, M. Review of experimental investigation on directly irradiated particles solar reactors. *Renew. Sustain. Energy Rev.* **2015**, *41*, 53–67. [CrossRef]
118. Jafarian, M.; Abdollahi, M.R.; Nathan, G.J. Preliminary evaluation of a novel solar bubble receiver for heating a gas. *Sol. Energy* **2019**, *182*, 264–277. [CrossRef]
119. Rodat, S.; Abanades, S.; Boujjat, H.; Chuayboon, S. On the path toward day and night continuous solar high temperature thermochemical processes: A review. *Renew. Sustain. Energy Rev.* **2020**, *132*. [CrossRef]
120. Rodat, S.; Abanades, S. A Hybrid Windowless Dual Tube Solar Reactor for Continuous Volumetric Natural Gas Dissociation. *Front. Energy Res.* **2020**, *8*. [CrossRef]
121. Rahimi, N.; Kang, D.; Gelinas, J.; Menon, A.; Gordon, M.J.; Metiu, H.; McFarland, E.W. Solid carbon production and recovery from high temperature methane pyrolysis in bubble columns containing molten metals and molten salts. *Carbon N. Y.* **2019**, *151*, 181–191. [CrossRef]
122. Upham, D.C.; Agarwal, V.; Khechfe, A.; Snodgrass, Z.R.; Gordon, M.J.; Metiu, H.; McFarland, E.W. Catalytic molten metals for the direct conversion of methane to hydrogen and separable carbon. *Science (80-)* **2017**, *358*, 917–921. [CrossRef]
123. Wang, K.; Li, W.S.; Zhou, X.P. Hydrogen generation by direct decomposition of hydrocarbons over molten magnesium. *J. Mol. Catal. A Chem.* **2008**, *283*, 153–157. [CrossRef]
124. Rowe, S.C.; Ariko, T.A.; Weiler, K.M.; Spana, J.T.E.; Weimer, A.W. Reversible Molten Catalytic Methane Cracking Applied to Commercial Solar-Thermal Receivers. *Energies* **2020**, *13*, 6229. [CrossRef]
125. Sakai, A.; Yamaguchi, F.; Kawazoe, T.; Yonemori, H.; Machida, Y. Process for Cracking Hydrocarbons Utilizing Amist of Molten Salt in the Reaction Zone. U.S. Patent 4,217,204, 12 August 1980.
126. Tokuji, O. Method and Appartus for Thermal Cracking and Quenching. U.S. Patent 3,718,708, 27 February 1973.
127. Dugan, J.; Israel, S.; PastrenaYao, K. Hydrocarbon Cracking in a Regenerable Molten Medium. U.S. Patent 3,876,527, 8 April 1975.
128. Oblad, A.G.; Milliken, T.H.; Boedeker, E.R. Production of Hydrogen and Carbon. U.S. Patent 2,760,847, 28 August 1956.
129. Leal Pérez, B.J.; Medrano Jiménez, J.A.; Bhardwaj, R.; Goetheer, E.; van Sint Annaland, M.; Gallucci, F. Methane pyrolysis in a molten gallium bubble column reactor for sustainable hydrogen production: Proof of concept & techno-economic assessment. *Int. J. Hydrog. Energy* **2020**. [CrossRef]
130. Zeng, J.; Tarazkar, M.; Pennebaker, T.; Gordon, M.J.; Metiu, H.; McFarland, E.W. Catalytic Methane Pyrolysis with Liquid and Vapor Phase Tellurium. *ACS Catal.* **2020**, *10*, 8223–8230. [CrossRef]
131. Kang, D.; Palmer, C.; Mannini, D.; Rahimi, N.; Gordon, M.J.; Metiu, H.; McFarland, E.W. Catalytic Methane Pyrolysis in Molten Alkali Chloride Salts Containing Iron. *ACS Catal.* **2020**, *10*, 7032–7042. [CrossRef]
132. Von Wald, G.A.; Masnadi, M.S.; Upham, D.C.; Brandt, A.R. Optimization-based technoeconomic analysis of molten-media methane pyrolysis for reducing industrial sector CO_2 emissions. *Sustain. Energy Fuels* **2020**, *4*, 4598–4613. [CrossRef]

133. Geißler, T.; Plevan, M.; Abánades, A.; Heinzel, A.; Mehravaran, K.; Rathnam, R.K.; Rubbia, C.; Salmieri, D.; Stoppel, L.; Stückrad, S.; et al. Experimental investigation and thermo-chemical modeling of methane pyrolysis in a liquid metal bubble column reactor with a packed bed. *Int. J. Hydrog. Energy* **2015**, *40*, 14134–14146. [CrossRef]
134. Serban, M.; Lewis, M.A.; Marshall, C.L.; Doctor, R.D. Hydrogen production by direct contact pyrolysis of natural gas. *Energy Fuels* **2003**, *17*, 705–713. [CrossRef]
135. Parkinson, B.; Patzschke, C.F.; Nikolis, D.; Raman, S.; Dankworth, D.C.; Hellgardt, K. Methane pyrolysis in monovalent alkali halide salts: Kinetics and pyrolytic carbon properties. *Int. J. Hydrog. Energy* **2021**, *46*, 6225–6238. [CrossRef]
136. Kang, D.; Rahimi, N.; Gordon, M.J.; Metiu, H.; McFarland, E.W. Catalytic methane pyrolysis in molten $MnCl_2$-KCl. *Appl. Catal. B Environ.* **2019**, *254*, 659–666. [CrossRef]
137. Patzschke, C.F.; Parkinson, B.; Willis, J.J.; Nandi, P.; Love, A.M.; Raman, S.; Hellgardt, K. Co-Mn catalysts for H2 production via methane pyrolysis in molten salts. *Chem. Eng. J.* **2021**, *414*, 128730. [CrossRef]
138. Engineers Edge—Reference Data for Engineers | GD&T ASME Training | GD&T Training | DFM DFA Training | Engineering Supplies Store | Engineering Tools for Productivity. Available online: https://www.engineersedge.com/ (accessed on 9 March 2021).
139. Periodic Table—Ptable. Available online: https://ptable.com/#Properties (accessed on 9 March 2021).
140. Palmer, H.B.; Hirt, T.J. The activation energy for the pyrolysis of methane. *J. Phys. Chem.* **1963**, *67*, 709–711. [CrossRef]
141. Gilliland, E.R.; Harriott, P. Reactivity of Deposited Carbon. *Ind. Eng. Chem.* **1954**, *46*, 2195–2202. [CrossRef]
142. Martynov, P.N.; Gulevich, A.V.; Orlov, Y.I.; Gulevsky, V.A. Water and hydrogen in heavy liquid metal coolant technology. *Prog. Nucl. Energy* **2005**, *47*, 604–615. [CrossRef]
143. Geißler, T.; Abánades, A.; Heinzel, A.; Mehravaran, K.; Müller, G.; Rathnam, R.K.; Rubbia, C.; Salmieri, D.; Stoppel, L.; Stückrad, S.; et al. Hydrogen production via methane pyrolysis in a liquid metal bubble column reactor with a packed bed. *Chem. Eng. J.* **2016**, *299*, 192–200. [CrossRef]
144. Kenney, C.N. Molten Salt Catalysis of Gas Reactions. *Catal. Rev.* **1975**, *11*, 197–224. [CrossRef]
145. Sada, E.; Kumazawa, H.; Kudsy, M. Pyrolysis of Lignins in Molten Salt Media. *Ind. Eng. Chem. Res.* **1992**, *31*, 612–616. [CrossRef]
146. Farmer, T.C.; McFarland, E.W.; Doherty, M.F. Membrane bubble column reactor model for the production of hydrogen by methane pyrolysis. *Int. J. Hydrog. Energy* **2019**, *44*, 14721–14731. [CrossRef]
147. Cahn, R.W.; Eustathopoulus, N.; Nicolas, M.; Drevet, B. *Wettability at High Temperatures*; Elsevier: Amsterdam, The Netherlands, 1999.
148. Ruuska, T.; Vinha, J.; Kivioja, H. Measuring thermal conductivity and specific heat capacity values of inhomogeneous materials with a heat flow meter apparatus. *J. Build. Eng.* **2017**, *9*, 135–141. [CrossRef]
149. Riley, J.; Atallah, C.; Siriwardane, R.; Stevens, R. Technoeconomic analysis for hydrogen and carbon Co-Production via catalytic pyrolysis of methane. *Int. J. Hydrog. Energy* **2021**. [CrossRef]
150. Baker, R.T.K. Catalytic growth of carbon filaments. *Carbon N. Y.* **1989**, *27*, 315–323. [CrossRef]
151. Takenaka, S.; Ogihara, H.; Otsuka, K. Structural Change of Ni Species in Ni/SiO_2 Catalyst during Decomposition of Methane. *J. Catal.* **2002**, *208*, 54–63. [CrossRef]
152. Goodwin, D.G.; Speth, R.L.; Moffat, H.K.; Weber, B.W. Cantera: An Object-Oriented Software Toolkit for Chemical Kinetics, Thermodynamics, and Transport Processes. Version 2.5.1. 2021. Available online: https://www.cantera.org (accessed on 15 January 2021).
153. Guil-Lopez, R.; Botas, J.A.; Fierro, J.L.G.; Serrano, D.P. Comparison of metal and carbon catalysts for hydrogen production by methane decomposition. *Appl. Catal. A Gen.* **2011**, *396*, 40–51. [CrossRef]
154. Zhou, L.; Enakonda, L.R.; Harb, M.; Saih, Y.; Aguilar-Tapia, A.; Ould-Chikh, S.; Hazemann, J.L.; Li, J.; Wei, N.; Gary, D.; et al. Fe catalysts for methane decomposition to produce hydrogen and carbon nano materials. *Appl. Catal. B Environ.* **2017**, *208*, 44–59. [CrossRef]
155. Younessi-Sinaki, M.; Matida, E.A.; Hamdullahpur, F. Kinetic model of homogeneous thermal decomposition of methane and ethane. *Int. J. Hydrog. Energy* **2009**, *34*, 3710–3716. [CrossRef]
156. Popov, M.V.; Bannov, A.G.; Brester, A.E.; Kurmashov, P.B. Effect of Temperature and Pressure on Conversion of Methane and Lifetime of the Catalyst in the Catalytic Decomposition of Methane. *Russ. J. Appl. Chem.* **2020**, *93*, 954–959. [CrossRef]
157. Pinilla, J.L.; Utrilla, R.; Karn, R.K.; Suelves, I.; Lázaro, M.J.; Moliner, R.; García, A.B.; Rouzaud, J.N. High temperature iron-based catalysts for hydrogen and nanostructured carbon production by methane decomposition. *Int. J. Hydrog. Energy* **2011**, *36*, 7832–7843. [CrossRef]
158. Rastegarpanah, A.; Meshkani, F.; Rezaei, M. Thermocatalytic decomposition of methane over mesoporous nanocrystalline promoted $Ni/MgO{\cdot}Al_2O_3$ catalysts. *Int. J. Hydrog. Energy* **2017**, *42*, 16476–16488. [CrossRef]
159. Zhang, W.; Ge, Q.; Xu, H. Influences of reaction conditions on methane decomposition over non-supported Ni catalyst. *J. Nat. Gas Chem.* **2011**, *20*, 339–344. [CrossRef]
160. Hurd, C.D.; Pilgrim, F.D. The Pyrolysis of Hydrocarbons. Further Studies on the Butanes. *J. Am. Chem. Soc.* **1933**, *55*, 4902–4907. [CrossRef]
161. Hurd, C.D.; Eilers, L.K. Pyrolysis Studies—Isobutylene, Diisobutylene, Ethylene, Propylene, and 2-Pentene. *Ind. Eng. Chem.* **1934**, *26*, 776–780. [CrossRef]
162. Crynes, B.L.; Albright, L.F. Pyrolysis of Propane in Tubular Flow Reactors. Kinetics and Surface Effects. *Ind. Eng. Chem. Process Des. Dev.* **1969**, *8*, 25–31. [CrossRef]